A novel analytical tool to capture wind profile variability for wind energy assessment: fast, simple, and beyond state-of-the-art in complex terrain

Brandon J.A. van Schaik[1], Alice J. Baruzier[1], Clément Loyer[1], Hendrik Huwald[1,2], and Michael Lehning[1,2]

[1]École Polytechnique Fédérale de Lausanne, EPFL ALPOLE Valais/Wallis, Route des Ronquoz 86, 1950 Sion, Valais, Switzerland

[2]WSL Institute for Snow and Avalanche Research SLF, Flüelastrasse 11, 7260 Davos, Graubünden, Switzerland

Correspondence: Brandon J.A. van Schaik (brandon.vanschaik@epfl.ch)

Abstract. Standardised wind turbine power-performance evaluation commonly represents the vertically varying rotor inflow by a single reference wind speed, such as hub-height wind speed or rotor-equivalent wind speed. Here, we present a computationally simple analytical rotor-integration model for turbine power that evaluates the vertical variation of horizontal wind speed using a Taylor expansion of the inflow velocity over the rotor disk. We assess idealised wind profiles to understand the isolated effects of typical shear, veer profiles, and turbulence on the power production of the turbine. This analytical model is then evaluated against power measurements from five Enercon E92 turbines at the Gotthard Pass, a complex-terrain wind park in the Swiss Alps, across 10 distinct wind events. The model consistently improves upon IEC-standard single-point extrapolations and reaches an accuracy comparable to OpenFAST simulations, while being at least 1000 times faster to compute, and requiring no specialised modelling expertise to operate. It thereby provides smoother and more accurate power estimates, reducing RMSE by 8.8 % and bias by 27.2 % relative to the IEC-standard approach. This equates to an annual energy production estimate that is 23.7 MWh closer to reality, for a 2.35 MW turbine at this complex terrain site. Additionally, it enables effective filtering of wake-affected LiDAR measurements, demonstrating flexibility, robustness, and applicability for pre-construction assessment and wind park expansion in complex terrain.

1 Introduction

Accurate modelling of wind turbine power generation requires more than the direct application of hub-height power curves. Standard power curves, as defined in IEC 61400-12-1, provide a well-established framework based on mean wind speed at hub height, but they only partly represent the atmospheric complexity that can influence power production (IEC, 2022; Sakagami et al., 2015). Remaining uncertainties are closely linked to wind variability, turbulence, and boundary-layer processes, whose effects become increasingly important as turbine size increases (Belu and Koracin, 2012).

Although multi-height wind measurements from meteorological masts and Doppler-wind LiDAR are widely used and included in international standards, power performance assessments typically reduce the vertically varying inflow across the

rotor-swept area to a single representative wind speed. This value is usually derived from a nacelle-mounted anemometer calibrated against the kinetic energy flux measured across the rotor plane approximately 2.5 rotor diameters upstream (IEC, 2022). While appropriate for standardised test sites with flat or mildly complex terrain, this approach assumes quasi-uniform inflow across the rotor disk. In complex terrain, however, strong vertical and lateral gradients caused by wind shear, directional veer, turbulence, yaw misalignment, and wake effects violate this assumption, leading to increased uncertainty in power curve application.

Turbulence intensity strongly influences measured power curves, as standard 10-minute averaging obscures short-term variability and complicates comparisons with guaranteed performance (Albers, 2010). Wind shear and directional veer further modify the effective inflow, such that alignment with hub-height wind may lead to sub- or super-optimal power production depending on the vertical profile (Murphy et al., 2020). These effects are amplified in complex terrain, where non-homogeneous upstream flow alters wake development and induction compared to flat, homogeneous conditions (Troldborg et al., 2022; Gasser et al., 2026). Despite these limitations, the reduction of spatially varying inflow to a single-point wind speed remains the prevailing standard for consistency in power assessment (IEC, 2022).

In recent years, simulations and analytical approaches that explicitly account for spatial wind velocity distributions have gained attention for their ability to capture key processes influencing turbine power output. Modified power curve and induction models incorporating wind shear, veer, turbulence intensity, and yaw misalignment improve power prediction accuracy by up to 51 % (Vahidzadeh and Markfort, 2019, 2020). Similarly, coupling actuator disk theory with blade-element models to resolve vertical shear and directional changes improves agreement with observed turbine power and reduces prediction errors (Mata et al., 2024). At the wind-farm scale, Gaussian process and random forest approaches further highlight the importance of accounting for wake-induced turbulence and vertical profile variability, showing good agreement with large-eddy simulations and observations (Niayifar and Porté-Agel, 2015; Clifton and Wagner, 2014).

Early power-performance studies showed that the sensitivity of measured power curves to atmospheric conditions partly reflects limitations in the reference wind-speed definition. Using multi-level measurements across the rotor layer, Elliott and Cadogan (1990) demonstrated that stratifying power curves by turbulence intensity yields substantially different outputs at identical hub-height wind speeds, largely due to systematic deviations between hub-height and disk-averaged wind speeds under low-turbulence, strongly sheared conditions. In such regimes, hub-height wind speed frequently overestimates disk-averaged velocity, indicating that single-point measurements can bias the inferred kinetic input and distort interpretations of power-curve scatter and apparent underperformance (Elliott and Cadogan, 1990).

Motivated by these findings, several studies proposed replacing hub-height wind speed with an equivalent or rotor-averaged wind speed that better represents rotor-integrated inflow. Simulation studies over flat terrain showed that electrical power correlates more strongly with Rotor Equivalent Wind Speed (REWS), derived from measurements across the swept area, than with hub-height wind speed, highlighting that identical hub-height values can correspond to substantially different rotor-layer kinetic energy (Wagner et al., 2009). A widely adopted formulation defines REWS by matching the kinetic energy flux through

the rotor, resulting in a cubic (energy-based) rotor-area weighting:

$$U_{eq} = \left(\sum_i u_i^3 \frac{A_i}{A} \right)^{1/3} \tag{1}$$

where u_i represents the wind speed measured within rotor-area segment i, A_i is the area of that segment, and A is the total rotor-swept area. In LiDAR-based applications, this energy-equivalent definition reduces power-curve scatter and yields a power coefficient consistent with the profile-integrated kinetic energy flux, rather than the hub-height approximation (Wagner et al., 2011).

As rotor-equivalent wind-speed methods gained wider adoption, their practical implementation became an important topic. The IEA Wind Annex 32 comparative exercise showed that applying the IEC-draft REWS procedure requires explicit choices in assigning rotor-area weights to discrete measurement heights, including the definition of segment areas and the treatment of measurements not located at rotor-tip elevations. Even for identical wind profiles, small but systematic differences in REWS were found across institutions due solely to variations in the segmentation and weighting approach, highlighting that REWS is not only a concept but also a method affecting reproducibility. The same study further showed that REWS-based power curves can differ substantially from hub-height-based curves, particularly under strong shear and low turbulence conditions, where inflow non-uniformity is most pronounced (Wagner et al., 2014).

Beyond shear-only corrections, several studies proposed veer- and turbulence-aware rotor-equivalent formulations to better represent the wind component normal to the rotor plane and its variability. In industry practice, "veer-aware" equivalent wind speeds apply a cosine projection of directional differences across the rotor, effectively down-weighting misaligned inflow (Antoniou et al., 2013). Choukulkar et al. (2016) developed an equivalent wind speed that combines rotor-area weighting with wind-speed and direction variability, accounting for turbulence intensity, directional shear, and flow misalignment. Similarly, Redfern et al. (2019) introduced a momentum-based rotor-equivalent wind speed with a veer correction by projecting wind vectors onto the turbine axis.

Field measurements confirm that intra-rotor flow variability can lead to substantial deviations from standard power curves. Combinations of wind shear and directional veer can induce power changes ranging from -19 % to +34 % relative to the nominal curve at a given hub-height wind speed (Mata et al., 2024). Differences between hub-height wind speed and REWS can exceed 70 kW, corresponding to up to 5 % of rated power for a single turbine (Murphy et al., 2020). These discrepancies can propagate to the wind-farm scale and may lead to significant instantaneous and cumulative power prediction errors, although their aggregate effect depends on how errors vary across turbines.

Ground-based Doppler wind LiDAR enables retrieval of wind speed and direction profiles across the rotor-swept area, allowing equivalent wind speeds to be derived based on kinetic energy flux rather than single-point measurements (Wagner et al., 2011). Although IEC 61400-12-1 acknowledges that non-uniform inflow, including shear and turbulence across the rotor, can bias power-performance measurements, standardised procedures primarily express these effects through weighted or equivalent reference wind speeds for power-curve evaluation (IEC, 2022). This provides a reproducible basis for certification and comparison, but leaves room for complementary analytical formulations that explicitly decompose how shear, veer, turbulence, and yaw misalignment affect the rotor-integrated power input, especially in complex terrain.

The benefit of adopting REWS over hub-height wind speed is not universal, as both can differ by less than 1 % under homogeneous conditions with weak shear, implying limited added value in such cases. However, larger deviations occur in complex terrain and atypical shear regimes, supporting the view that REWS-based normalisation is most relevant where strong, non-linear shear and veer are frequent conditions typical of mountainous wind parks and central to this study (Van Sark et al., 2019).

Building on this established body of work, the present study does not aim to introduce rotor-equivalent wind speed or rotor-integrated inflow concepts as new. Instead, we develop a computationally simple analytical formulation that evaluates wind turbine power generation directly as an integral over the rotor-swept area. The formulation retains the physical interpretation of rotor-integrated kinetic energy while allowing the separate and combined effects of vertical shear, directional veer, turbulence intensity, and yaw misalignment to be evaluated explicitly. The contribution of the study therefore lies in the specific analytical implementation, its comparison against OpenFAST simulations under controlled inflow conditions, and its application to LiDAR-derived wind profiles from the complex-terrain Gotthard Pass field site.

To evaluate the proposed analytical approach, we use numerical simulations from OpenFAST, an open-source wind turbine model developed by National Laboratory of the Rockies (NRL), formerly known as National Renewable Energy Laboratory (NREL) (Jonkman, 2013), which resolves turbine dynamics under spatially and temporally varying inflow and captures the intra-rotor flow structure considered here.

The analysis focuses on a mountainous site with complex terrain at the Gotthard Pass in the Swiss Alps. During a field campaign, wind profiles were measured using LiDAR, providing observations of vertically variable flow conditions relevant for wind-turbine power estimation in complex terrain.

This article is structured as follows. Sec. 2 summarises the established theoretical and experimental background needed for the study, including rotor-equivalent wind-speed concepts, the turbine power equation, turbulence notation, the Gotthard field site, and the OpenFAST/TurbSim framework. Sec. 3 then describes the specific implementation developed here: the Taylor-series rotor integration, the power-curve and power-coefficient retrieval, the idealised profile experiments, the OpenFAST sensitivity simulations, and the application to LiDAR-derived Gotthard inflow profiles. The results then compare the analytical estimates with the numerical simulations and measured turbine power to assess when vertical profile information improves power prediction in complex terrain.

2 Background and theoretical framework

This section summarises the established concepts and data sources on which the present method is built. The material is separated from the implementation of the proposed method so that the analytical assumptions, site information, and numerical modelling framework are introduced before the workflow used in this study.

2.1 Rotor-equivalent wind speed and turbine power

The standard wind turbine power equation can be written as

$$P(U_{eq}) = \frac{1}{2} C_p(U_{eq}) \rho A U_{eq}^3, \tag{2}$$

where P is the turbine power output, U_{eq} is a representative rotor-equivalent wind speed, C_p is the power coefficient, ρ is air density, and $A = \pi R^2$ is the rotor-swept area with rotor radius R. In the simplest interpretation, U_{eq} is represented by the hub-height wind speed. In rotor-equivalent wind-speed approaches, however, U_{eq} is instead derived from the kinetic-energy flux through the rotor-swept area, for example using Eq. 1.

Eq. 2 is therefore not introduced here as a new model, but as the basis from which rotor-integrated approaches follow. The contribution of this study is to retain the rotor-integrated interpretation while expressing the vertical inflow profile as an analytical function. This makes it possible to decompose the effects of shear, veer, and turbulence without reducing all inflow variability to a single scalar wind speed at the start of the calculation.

2.2 Vertical inflow variability

In complex terrain, wind velocity varies across the rotor-swept area due to terrain-induced acceleration, directional channelling, vertical shear, turbulence, and wake effects. In undisturbed boundary-layer flow, vertical variations are generally more important than horizontal variations across the rotor disk, because vertical gradients in wind speed and direction are a dominant feature of the surface layer and lower boundary layer (Stull, 1988; Wagner et al., 2014; IEC, 2022). This assumption does not necessarily hold inside turbine wakes or in strongly heterogeneous terrain-induced flow; wake-contaminated profiles are therefore treated separately in Sect. 4.3.

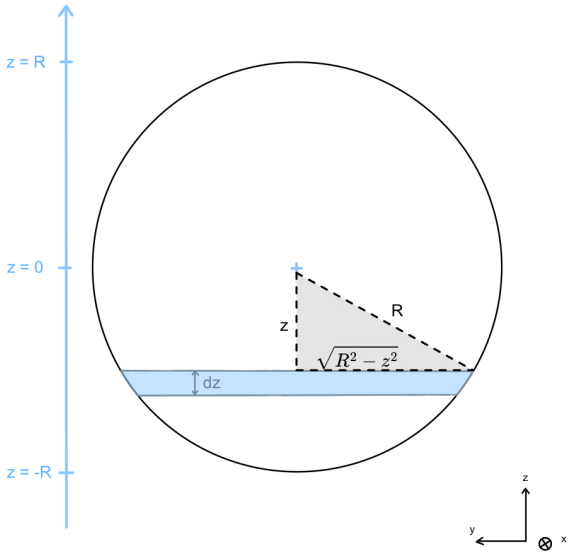


Figure 1. Vertical integration over the rotor-swept area of a wind turbine.

As shown in Fig. 1, the coordinate z is defined relative to the turbine hub, with $z = 0$ at hub height and $z = -R$ and $z = R$ at the lower and upper rotor tips. A vertical profile $v(z)$ therefore describes the horizontal wind-speed magnitude sampled through the rotor layer. Directional veer is treated by projecting the wind vector onto the rotor-normal direction before applying the same vertical integration.

2.3 Turbulence notation

For the analytical turbulence treatment, turbulence is represented by the second-order statistics of the wind speed at each measurement height. For each height z, the 10-minute wind-speed distribution is described by a mean $\bar{v}(z)$ and standard deviation $\sigma_v(z)$. These are not rotor-equivalent quantities; they are height-dependent statistics derived from the measured or prescribed wind-speed time series. The latter is derived directly from the WindCube LiDAR wind speed dispersion parameter as described in VAISALA (2023).

In the analytical implementation, the instantaneous wind speed at height z is approximated by a Gaussian distribution,

$$f_z(V) = \frac{1}{\sqrt{2\pi\sigma_v(z)^2}} \exp\left[-\frac{(V - \bar{v}(z))^2}{2\sigma_v(z)^2}\right], \tag{3}$$

where V denotes the instantaneous wind speed used as the integration variable. The Gaussian assumption is used here as a controlled second-order representation of turbulent wind-speed variability. Rather than attempting to reproduce all higher-order or non-Gaussian features of atmospheric turbulence, it provides a reproducible and analytically tractable formulation that can be directly combined with the turbine power curve.

van Schaik et al. (2025b) showed that heavier-tailed wind-speed distributions, such as the Student's t-distribution, are commonly observed at the Gotthard Pass. In the present formulation, however, turbulence is represented through a single standard-deviation measure. Within this second-order framework, the effect of heavier tails can be incorporated through a simple scaling of the wind-speed standard deviation by a factor of 1.81, which effectively captures their influence on turbine power output (van Schaik et al., 2025b).

2.4 Gotthard field site and observations

The observational evaluation uses the Gotthard Wind Park in the central Swiss Alps. The wind farm is located at 2106 m a.m.s.l. on the north–south-oriented Gotthard Pass and consists of five Enercon E92 wind turbines with a rated power of 2.35 MW, a hub height of 98 m, and a rotor diameter of 92 m. Real-condition wind power output and nacelle wind-speed data at 10-minute resolution were taken from van Schaik et al. (2025b).

During the Gotthard transect campaign, Doppler wind LiDAR measurements were collected at several locations around the wind farm. The LiDAR measured vertical profiles of wind speed, wind direction, and wind-speed variability at 10-minute resolution, with measurement heights of 40–150 m in 10 m increments and 160–300 m in 20 m increments. For the Enercon E92 rotor layer, this provides typically 6–9 measurement gates within the rotor-swept area, depending on the LiDAR location and local elevation difference relative to the turbine base.

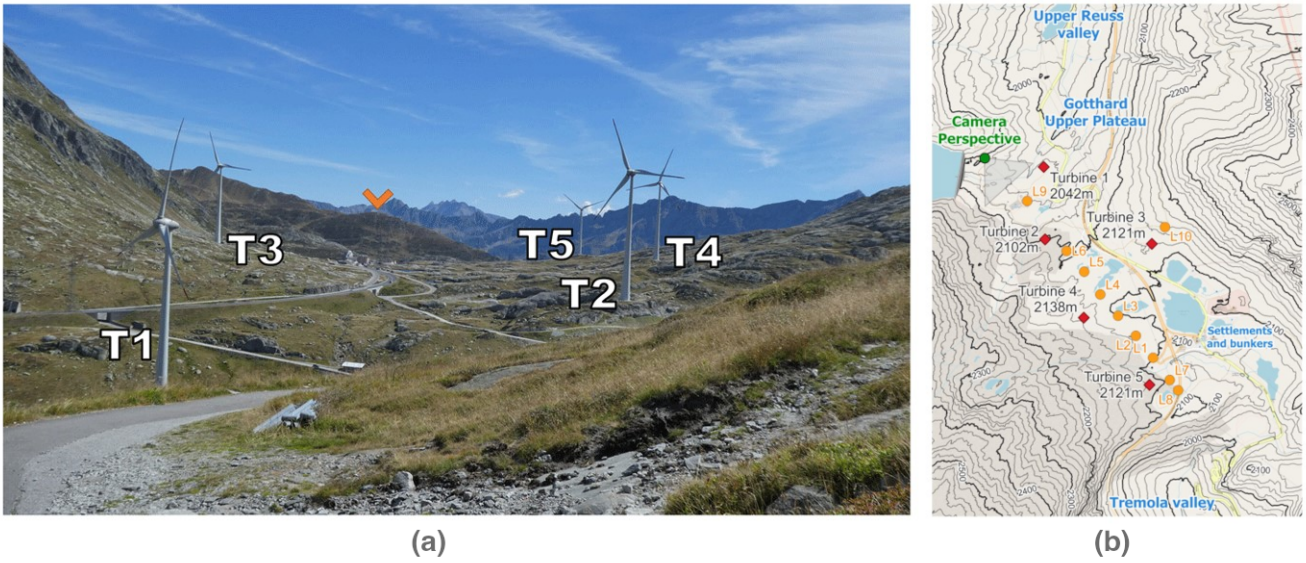


Figure 2. Turbine and LiDAR locations from the Gotthard Doppler wind LiDAR campaign in summer 2023, adapted from van Schaik et al. (2025b).

2.5 OpenFAST and TurbSim background

OpenFAST is used as a numerical reference framework to test the analytical formulation under controlled inflow conditions. Because the detailed blade geometry and controller configuration of the Enercon E92 are proprietary, the simulations use the open-source WindPACT 3.0 MW reference turbine. This introduces a known limitation: differences between the Enercon E92 and WindPACT power curves can affect the comparison independently of the inflow-integration method.

TurbSim is used only to generate the inflow fields required by OpenFAST. Non-turbulent simulations use deterministic user-defined vertical wind profiles and do not rely on a physically meaningful turbulence spectrum. Turbulent simulations use the user-defined von Kármán spectral option, USRVKM, for which vertical profiles of mean wind speed, wind-speed standard deviation, and integral length scale can be prescribed. The integral length scale controls the spatial coherence and size of the energy-containing eddies in the generated inflow field. Because LiDAR profiles provide $\bar{v}(z)$ and $\sigma_v(z)$, but do not directly prescribe a unique three-dimensional integral length-scale profile, the choice of length scale introduces an additional modelling uncertainty. However, effective integral length scales can be estimated from the high-frequency LiDAR data by computing the autocorrelation of the beam-wise velocity fluctuations and converting the resulting integral timescale to a length scale using Taylor's frozen-turbulence hypothesis. The treatment and sensitivity of these length-scale and component-scaling parameters are therefore discussed in detail in Sec. 3.5, Sec. 4.4, and App. B.

3 Methodology

This section describes the implementation used in this study. The workflow consists of (i) fitting Taylor polynomials to the vertical mean and turbulence profiles, (ii) retrieving an analytical turbine power curve and the corresponding power coefficient, (iii) applying the analytical rotor integration to idealised profiles, (iv) comparing with OpenFAST simulations and sensitivity experiments, and (v) applying the same workflow to the measured Gotthard LiDAR profiles.

3.1 Analytical rotor integration

To account for vertical variations in horizontal wind speed, the power input is integrated over horizontal rotor slices, as shown in Fig. 1. The width of a slice at height z is $2\sqrt{R^2 - z^2}$, giving

$$P_{an} = \frac{1}{2} C_p(U_{eq}) \rho \int_{-R}^{R} 2\sqrt{R^2 - z^2}\, v(z)^3 \, \mathrm{d}z. \tag{4}$$

Here, $v(z)$ is the vertical profile of horizontal wind speed after any required vector projection onto the rotor-normal direction. The power coefficient is evaluated at the rotor-equivalent wind speed corresponding to the same profile, not independently at each height.

The measured or idealised profile is represented by a Taylor polynomial of order N,

$$v(z) = \sum_{i=0}^{N} c_{v,i} z^i = c_{v,0} + c_{v,1} z + c_{v,2} z^2 + \ldots + c_{v,N} z^N. \tag{5}$$

The notation $c_{v,i}$ is used to distinguish the Taylor coefficients of the mean wind-speed profile from the turbulence-profile coefficients introduced below. In the present study, $N = 3$ is used as a compromise between flexibility and overfitting. The same order is used for all measured and idealised profiles unless stated otherwise.

Substituting Eq. 5 into Eq. 4 gives an analytical expression for the rotor-integrated power,

$$P_{an} = \frac{1}{2} C_p(U_{eq}) \rho A \sum_{i,j,k=0}^{N} c_{v,i} c_{v,j} c_{v,k} R^m K_m, \quad m = i + j + k, \quad m \text{ even}, \tag{6}$$

with

$$K_m = \frac{m!}{2^m \left[(m/2)!\right]^2 (m/2+1)}. \tag{7}$$

Odd values of m do not contribute because the corresponding terms integrate to zero over the symmetric rotor interval. The full derivation is provided in App. A. In the code implementation, the workflow first fits $c_{v,i}$ from the available height levels and then evaluates Eq. 6 exactly through the triple summation.

3.2 Power-curve fitting and power-coefficient retrieval

The analytical model requires both a continuous turbine power curve and the corresponding power coefficient. The turbine power curve is represented by

$$P_{pc}(U) = P_r \left[1 - \exp\left(- \left(\frac{U - v_{in}}{C} \right)^B \right) \right], \tag{8}$$

for $v_{in} \leq U \leq v_{out}$, with $P_{pc} = 0$ below cut-in and above cut-out and $P_{pc} = P_r$ in the rated-power region where applicable. The fixed parameters v_{in}, v_{out}, and P_r are taken from the turbine technical specifications wind-turbine-models.com (2026). The shape parameters B and C are fitted to the published power-curve table, which results in the fit of Fig. 3, which gives an excellent agreement with the tabulated manufacturer power curve.

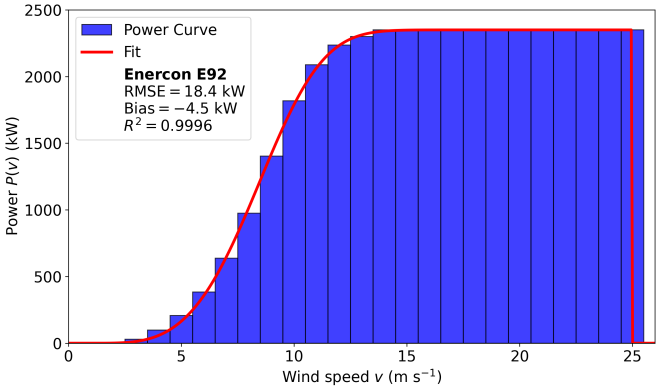


Figure 3. Fitting of Eq. 8 to the Enercon E92 2.35 MW turbine.

After fitting $P_{pc}(U)$, the corresponding power coefficient is computed as

$$C_p(U) = \frac{2P_{pc}(U)}{\rho A U^3}. \tag{9}$$

This makes the output of the power-curve-fitting step explicit: the fitted power curve $P_{pc}(U)$ and the derived power coefficient $C_p(U)$ are both passed to the analytical rotor-integration workflow. For the Gotthard application, the Enercon E92 2.35 MW power curve is used. For the OpenFAST comparison, the WindPACT 3.0 MW reference-turbine power curve is kept separate so that differences in turbine design are not confused with differences in inflow treatment. The exact specifications of both turbines can be found in Tab. 1.

Table 1. Specifications of the Enercon E92 and NREL WindPACT turbines in this study.

Turbine	**Enercon E92**	**NREL WindPACT**
Location	Gotthard pass	OpenFAST
Blade diameter $[\mathrm{m}]$	92	100
Nacelle height $[\mathrm{m}]$	98	119
Rated power $[\mathrm{kW}]$	2350	3000
Rated wind speed $[\mathrm{m\,s^{-1}}]$	14	12
Cut-in wind speed $[\mathrm{m\,s^{-1}}]$	2	1
Cut-out wind speed $[\mathrm{m\,s^{-1}}]$	25	None
Air density $[\mathrm{kg\,m^{-3}}]$	0.996	0.996

3.3 Analytical treatment of turbulence

For turbulent inflow, the mean wind-speed profile and the wind-speed standard-deviation profile are both represented over the rotor layer. The two fitted profiles are given in Eq. 5 and Eq. 10

$$\sigma_v(z) = \sum_{i=0}^{N} c_{\sigma_v,i} z^i, \tag{10}$$

where $c_{v,i}$ and $c_{\sigma_v,i}$ are the Taylor coefficients returned by the Taylor-expansion step.

At each height, the expected power under turbulent wind-speed fluctuations is computed by integrating the fitted turbine power curve over the local Gaussian wind-speed distribution given by Eq. 3,

$$\langle P \rangle_z = \int_{v_{in}}^{v_{out}} P_{pc}(V) f_z(V)\,\mathrm{d}V. \tag{11}$$

The rotor-integrated turbulent-power estimate is then,

$$P_{turb} = \int_{-R}^{R} 2\sqrt{R^2 - z^2}\,\langle P \rangle_z\,\mathrm{d}z. \tag{12}$$

We then refer to the contribution of turbulence to the power output of the wind turbine as the difference between this estimate and the non-turbulent estimate based on the same mean profile,

$$\Delta P_{turb} = P_{turb} - P_{an}(\bar{v}). \tag{13}$$

This distinction avoids ambiguity between the absolute expected power in turbulent conditions and the deviation caused by turbulence. Positive values of ΔP_{turb} occur mainly in the convex part of the power curve, while negative values occur where the power curve is concave.

3.4 Idealised wind-profile experiments

Idealised profiles are used to isolate the effects of vertical shear, veer, turbulence, and logarithmic wind-speed structure. For each experiment, both the mean wind-speed profile and the turbulence profile are specified explicitly. In Fig. 4, the three different wind profiles are shown: linear-shear, linear-veer, and logarithmic profiles are first evaluated without turbulence, i.e. with $\sigma_v(z) = 0$ at all heights. The logarithmic wind-speed profile is written as

$$v(z) = \frac{u_*}{\kappa} \ln\left(\frac{z_h + z}{z_0}\right), \tag{14}$$

where u_* is friction velocity, κ is the von Kármán constant, z_h is hub height, and z_0 is aerodynamic roughness length. This profile is used as an idealised boundary-layer case and not as a fitted site-specific roughness estimate. The homogeneous-turbulence experiment is evaluated using a uniform mean wind-speed profile and constant turbulence intensity over the rotor layer. All of these wind profiles are compared to a uniform wind profile where $v(z)$ is constant with height and $\sigma_v(z) = 0$.

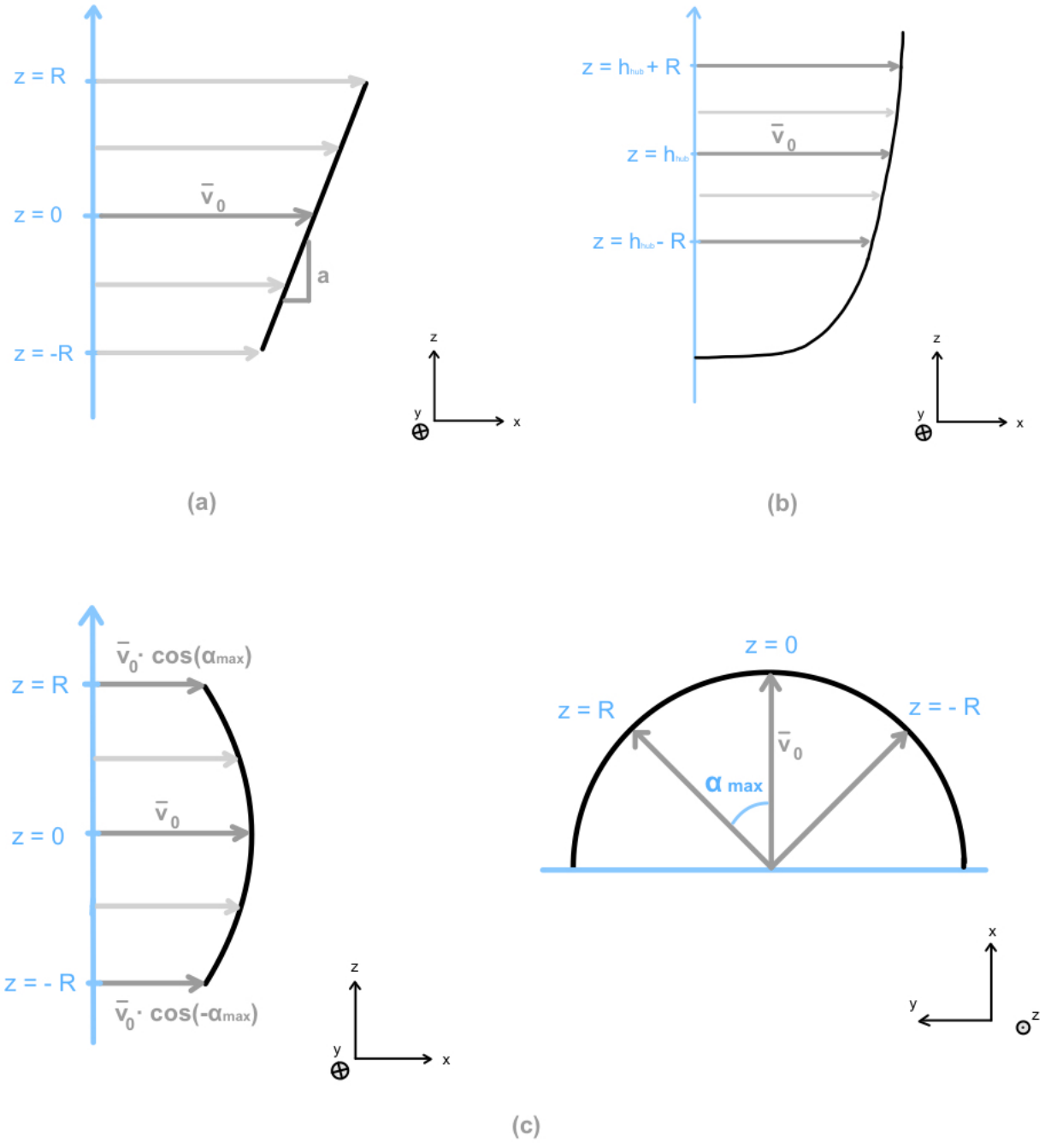


Figure 4. Examples of the idealised vertical wind profiles (a) linear shear, (b) logarithmic wind profile, and (c) linear veer.

For a given idealised profile, the analytical power deviation is computed relative to a uniform reference profile with the same hub-height wind speed,

$$\Delta P = P_{profile} - P_{ref}. \tag{15}$$

3.5 OpenFAST simulations and sensitivity analysis

OpenFAST simulations are used to test whether the analytical response to prescribed vertical profiles is consistent with the analytical turbine model. All simulations use the WindPACT 3.0 MW reference turbine because a complete open aeroelastic model of the Enercon E92 is not available. Simulations are run for 12 min, with the first 2 min discarded as spin-up and the final 10 min used for comparison with the standard averaging interval of the LiDAR and turbine data.

For non-turbulent simulations, deterministic user-defined profiles are supplied without invoking a stochastic turbulence spectrum. For turbulent simulations, TurbSim is used with the USRVKM option, defined here as the user-defined von Kármán spectral model. In this configuration, the measured or prescribed $\bar{v}(z)$ and $\sigma_v(z)$ profiles are supplied directly, while the integral length-scale profile and component scaling must be prescribed separately. In the OpenFAST setup, these parameters are kept at the standard values of the TurbSim USRVKM example file, with $L = [3, 4, 6, 9, 13, 13, 13, 13, \ldots]$ m at successive 10 m height increments and component scaling $(1.092, 1.000, 0.534)$ in the streamwise, cross-streamwise, and vertical directions, respectively. These parameters control the spatial coherence and characteristic size of the energy-containing eddies in the synthetic turbulent inflow field.

These example settings are not interpreted as physically representative atmospheric integral length scales for the Gotthard Pass inflow conditions. In particular, the short length-scale profile is part of an example input configuration rather than a site-specific turbulence parameterisation. However, effective integral length scales can be estimated from the high-frequency LiDAR data and used to define a physically motivated sensitivity case. The methodology for deriving this LiDAR-based length-scale profile and component scaling is described in App. B, while its influence on the results is presented in Sec. 4.4.

As shown later in Sec. 4.4, and relevant for the methodological choices made here, the lidar-derived estimates show substantial variability, with individual 10-minute length-scale estimates ranging from a few metres to several hundred metres depending on height, component, and inflow period. This variability indicates that there is no single objectively correct length-scale profile for all simulated cases. Prescribing a separate length-scale profile and component scaling for each individual inflow period would introduce an additional, poorly constrained degree of freedom in the OpenFAST comparison and would shift the focus of the analysis towards turbulence parameterisation in TurbSim. Therefore, the original USRVKM example settings are retained as the baseline numerical configuration, while the LiDAR-derived estimates are used to motivate an order-of-magnitude length-scale sensitivity case. The purpose of this additional analysis is not to recalibrate TurbSim uniquely for each individual inflow period, but to test whether the conclusions depend on the order of magnitude of the prescribed turbulent length scale and on the component scaling.

This sensitivity analysis reflects the role of eddy scale in the present study. The analytical model does not attempt to resolve the instantaneous three-dimensional structure of individual eddies, but represents turbulence statistically through the measured variance profile $\sigma_v(z)$ and the local curvature of the power curve. Over a 10-minute averaging period, the inflow advects over

several kilometres, so the turbine samples many turbulent structures with different sizes, phases, and rotor positions. The length scale and coherence of these structures can affect individual OpenFAST realisations, but part of this variability is expected to average out in the 10-minute mean.

3.6 Application to Gotthard LiDAR profiles

The measured LiDAR profiles are processed in the same way as the idealised profiles. For each 10-minute time step, the measured mean wind-speed profile $\bar{v}(z)$ and, where used, the measured wind-speed standard-deviation profile $\sigma_v(z)$ are fitted with Taylor polynomials of order $N = 3$. The resulting coefficients are passed to the analytical rotor-integration model.

For the OpenFAST comparison, the same LiDAR profiles are transformed from the Enercon E92 rotor geometry to the WindPACT 3.0 MW rotor geometry. The height transformation is

$$z_{new} = \frac{R_{WP3.0}}{R_{E92}} \left(z_{old} + \Delta z_{lidar} - h_{E92} \right) + h_{WP3.0}, \tag{16}$$

which gives, for $R_{WP3.0} = 50$ m, $R_{E92} = 46$ m, $h_{WP3.0} = 119$ m, and $h_{E92} = 98$ m,

$$z_{new} = \frac{50}{46} \left(z_{old} + \Delta z_{lidar} - 98 \right) + 119. \tag{17}$$

Here, z_{old} is the original LiDAR measurement height relative to the LiDAR base, Δz_{lidar} is the elevation difference between the LiDAR and turbine base, and z_{new} is the corresponding height in the WindPACT coordinate system. This form avoids introducing an unexplained fitted constant and can be adapted directly to other turbine geometries.

For each turbine and each prevailing wind direction, a nearby upwind LiDAR deployment is selected. Four-hour windows are used where data availability allows, yielding 10-minute profile–power pairs for comparison with the corresponding turbine production data. The OpenFAST power output is scaled by the rated-power ratio $2.35/3.0$ only for comparison with the Enercon E92 measurements; this scaling is stated explicitly as a pragmatic comparison step rather than as a claim of aerodynamic equivalence between the turbines. A summary of the complete methodology pipeline is shown in Fig. 5.

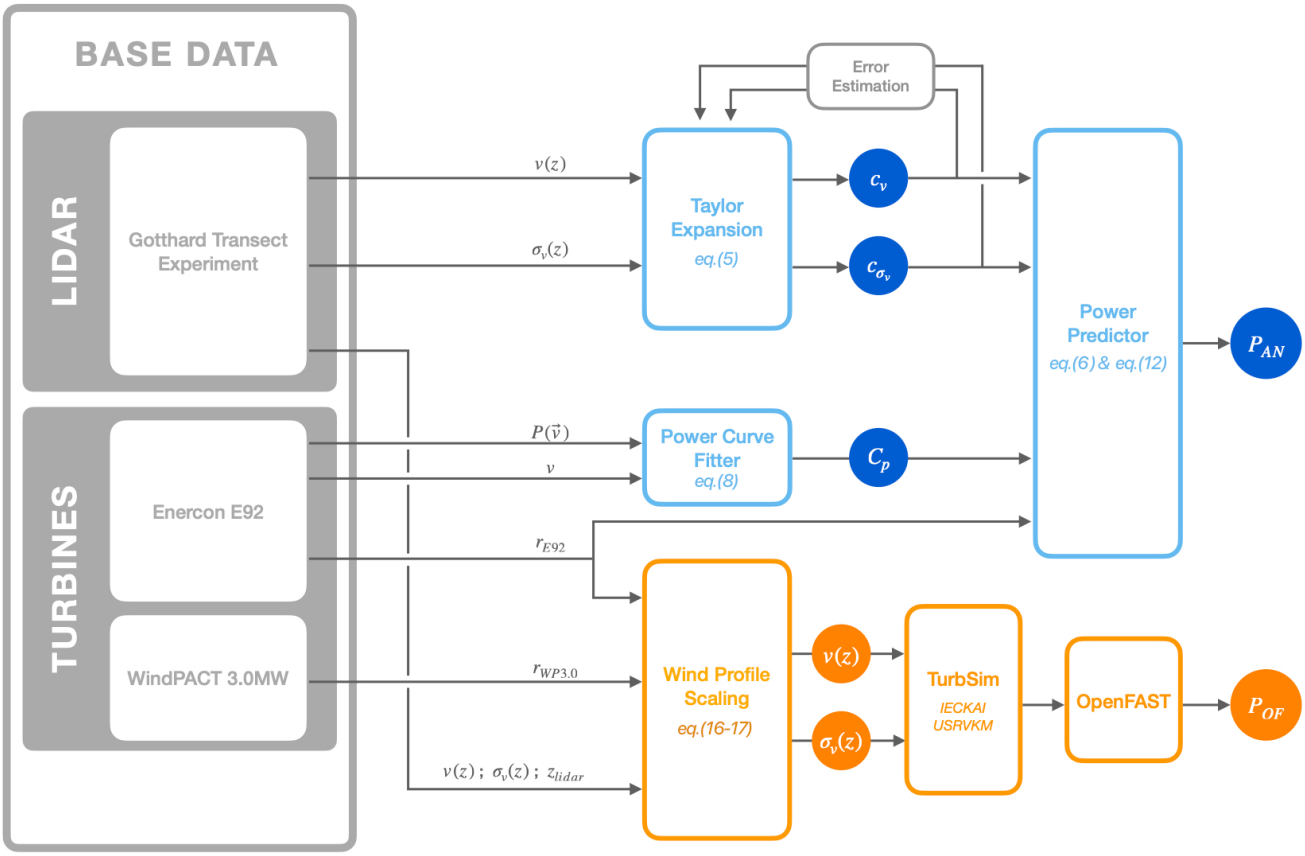


Figure 5. Schematic of the analytical and OpenFAST model workflow. The power-curve fitter returns both $P_{pc}(U)$ and $C_p(U)$; the Taylor-expansion step returns coefficients for both the mean wind-speed profile, c_v, and the wind-speed standard-deviation profile, c_{σ_v}, when turbulence is included.

3.7 Model evaluation and wake filtering

Model predictions are evaluated against the measured 10-minute power production of the five Enercon E92 turbines. Each turbine is considered separately for northerly and southerly flow, giving 10 validation cases. The primary case-wise metric is bias. Across the wake-free cases, RMSE, MAE, and the coefficient of determination are computed from the original unbinned 10-minute data. Binned curves are used only for visualisation and not as the basis for goodness-of-fit statistics.

Wake-contaminated profiles are treated separately. When a LiDAR range gate is clearly affected by a turbine wake but adjacent measurements remain representative of the undisturbed profile, the affected gates can be removed before fitting the

Taylor polynomial. The analytical model is then applied to the reconstructed profile. This filtering is used only as a diagnostic test of the method's flexibility and is not included in the main wake-free model-performance statistics.

4 Results and discussion

The following results assess the performance of the newly derived analytical model against both the IEC standard methods and high-fidelity OpenFAST simulations. Traditionally, the IEC standard approach relies on a single-point wind speed measurement, taken either at nacelle height or scaled from two-thirds of nacelle height, which neglects vertical wind profile variations. Our analytical model aims to overcome this limitation by explicitly accounting for vertical wind structure, while remaining computationally efficient.

We begin by isolating the effects of typical features of vertical wind profiles, which includes shear, veer, and logarithmic wind profiles, as well as homogeneous turbulence intensity, through the idealised wind profile test cases. We then apply the model to ten real-world cases applied to the five turbines at the Gotthard Pass, distinguishing between northerly and southerly flow conditions. Finally, we highlight one case strongly affected by wake interactions, and demonstrate how wake filtering can be applied to recover the undisturbed power signal and improve power prediction significantly.

4.1 Idealised wind profiles

The comparison between the power expectation from OpenFAST and the analytical model is summarised in Fig. 6. For linear shear (Fig. 6a), we find that shear effects contribute positively to the power production of the turbine in comparison to the homogeneous wind profile. The power estimated by the OpenFAST model consistently increases with shear, reflecting the cubic dependence of power on wind speed ($P \propto v^3$), where higher wind speed contribute more significantly to the overall output. Above the rated wind speed, ΔP tends to 0 as the turbine saturates at its maximum capacity and the extra wind speed is not able to positively contribute to the power production. This is particularly well illustrated by the sudden drop of the OpenFAST curve at $v = 12\ \mathrm{m\ s^{-1}}$. For the analytical model, the rated power is reached more smoothly at $v = 14\ \mathrm{m\ s^{-1}}$ which can directly be attributed to the smoother curvature of the power curve as reported in Sec. 4.1.1. With increasing shear coefficient a, we see similar increases in magnitude of ΔP for both models, and the peak values scale as expected with $\propto a^2$ as described in Eq. 18.

$$\Delta P_{\text{shear}} = \frac{3}{4} \cdot \frac{R^2 a^2}{v_0^2} \cdot P_{\text{ref}} \tag{18}$$

Where $a = 0.01/0.025/0.05\,[\mathrm{s^{-1}}]$ is the shear coefficient, and $z = 0$ is defined at the nacelle of the turbine. Fig. 4a illustrates the shear parameter across the rotor area.

Concerning the differences in the two models, we can observe two elements: the apparent overestimation of the analytical model, and the linear behaviour of the OpenFAST curve for low velocities. The overestimation of the power difference in the analytical model is most likely caused to the several reducing factors not taken into account in the analytical model. For

example, the OpenFast considers the reduced efficiency of energy transfer from the wind to the turbine blade due to non-ideal angle of attack. Additional shearing forces and vibrations, that will inevitably cause additional friction and reduced power production in reality.

In the case of linear veer, shown in Fig. 6b, the observations are analogous to the shear, but lead to a reduction in power output instead of an increase. This reduction arises from the diminished effective wind velocity component normal to the rotor plane, which is caused by the veer angle. The shape of both power difference curves are similarly more abrupt for the OpenFAST model due to the less refined and realistic power curve, and the analytical model reports higher differences due to a lack of dampening factors that are present in OpenFAST. As we vary the maximum veer angle $\alpha_{\max}$, the analytical model follows the expected square dependence ($\Delta P \propto \alpha_{\max}^2$) as described in Eq. 19.

$$\Delta P_{\text{veer}} = -\frac{3}{8} \cdot \alpha_{\max}^2 \cdot P_{\text{ref}} \tag{19}$$

where $\alpha_{\max} = \alpha R = 5/10/22.5\,[^\circ]$ is the maximum angular deviation at the upper and lower extents of the rotor-swept area. Fig. 4c shows the definition of this veer parameter.

The OpenFAST simulations, however, show slightly different magnitudes, with relatively larger power losses at smaller angles ($\alpha_{\max} = 5^\circ$) and smaller losses at larger angles ($\alpha_{\max} = 22.5^\circ$). This deviation is most likely due to the more detailed modelling of airflow over the blades, but it remains of secondary importance compared to the dominant quadratic dependence on $\alpha_{\max}$ in determining the overall turbine power output.

The ΔP curves of homogeneous turbulence, shown in Fig. 6c, have a characteristic shape: such a relationship between power curve curvature and power contributions related to turbulence has been previously described by Gasser et al. (2026). For low wind speeds, up to the inflection point of the power curve, turbulence tends to increase power production. This is because the turbulence velocity distribution, which is symmetric up to second order, places greater weight on velocity realisations above the mean. This holds true for the region in the power curve where the curvature is convex (i.e. positive in Fig. 7b), these higher velocities contribute disproportionately to the average power. Beyond the inflection point, however, the situation is reversed: the turbine response starts to saturate and the contribution of velocities below the mean becomes more significant than that of velocities above it. As a result, the net effect of turbulence is a reduction in power output.

The behaviour at the tail of the curve differs markedly between the two approaches. While the analytical model predicts no change in mean power above rated wind speed, the OpenFAST simulations show a small linear reduction. This behaviour is most plausibly explained by control-system and actuator dynamics under high turbulence: rapid fluctuations in effective angle of attack lead to persistent pitch-tracking errors (due to sensor/estimator lag, pitch-rate and torque limits, and anti-wind-up). The controller likely simulates the rotor speed varying above and below the rated speed, where the power is clipped to a maximum on the positive variations, but not on the negative ones. The result is a small shortfall from the rated power set point that increases with turbulence intensity. Although our field dataset contains limited observations above rated wind speed, previous studies show that modern pitch-regulated turbines are designed to maintain constant power in this regime through active control adjustments (Rosmin et al., 2010; Sedaghat et al., 2016).

As we vary the turbulence intensity (TI), the magnitude of the turbulence-induced power variations increases in proportion to the second derivative of the power curve, as expected for both the analytical and OpenFAST models. A slight exception occurs for the OpenFAST model near the peak positive contribution to wind power around $v = 9.5$. With increasing TI, this peak shifts toward slightly lower wind speeds. This behaviour is likely due to the more detailed modelling of the flow over the turbine blades in OpenFAST and represents a secondary effect.

The final idealised profile which we will discuss is the logarithmic profile shown in Fig. 6d, a common profile that is used to describe the standard wind shear of the earth's surface. The curvature effects previously described for the linear shear still hold in this simulation. A noticeable observation is the relatively low impact of the logarithmic profile, with the maximum deviation from the uniform inflow amounting to only about 15 kW and 20 kW for the Analytical and OpenFAST models, respectively. The logarithmic profile resembles the linear shear profile in shape, however the increase in wind speed is more strongly limited than the decrease. So instead of a net positive effect, as might be expected from the convexity of the power curve, it results in a small negative effect. As discussed earlier in this Section, OpenFAST predicts this behaviour more abruptly, while the analytical model responds more smoothly. Interestingly, in this case the analytical model predicts a smaller magnitude of change. This is likely because, in the analytical formulation, the positive contributions more strongly compensate for the negative ones, whereas OpenFAST still simulations have additional sources of power loss due to friction and control dynamics of the turbine, compared to the baseline OpenFAST simulation.

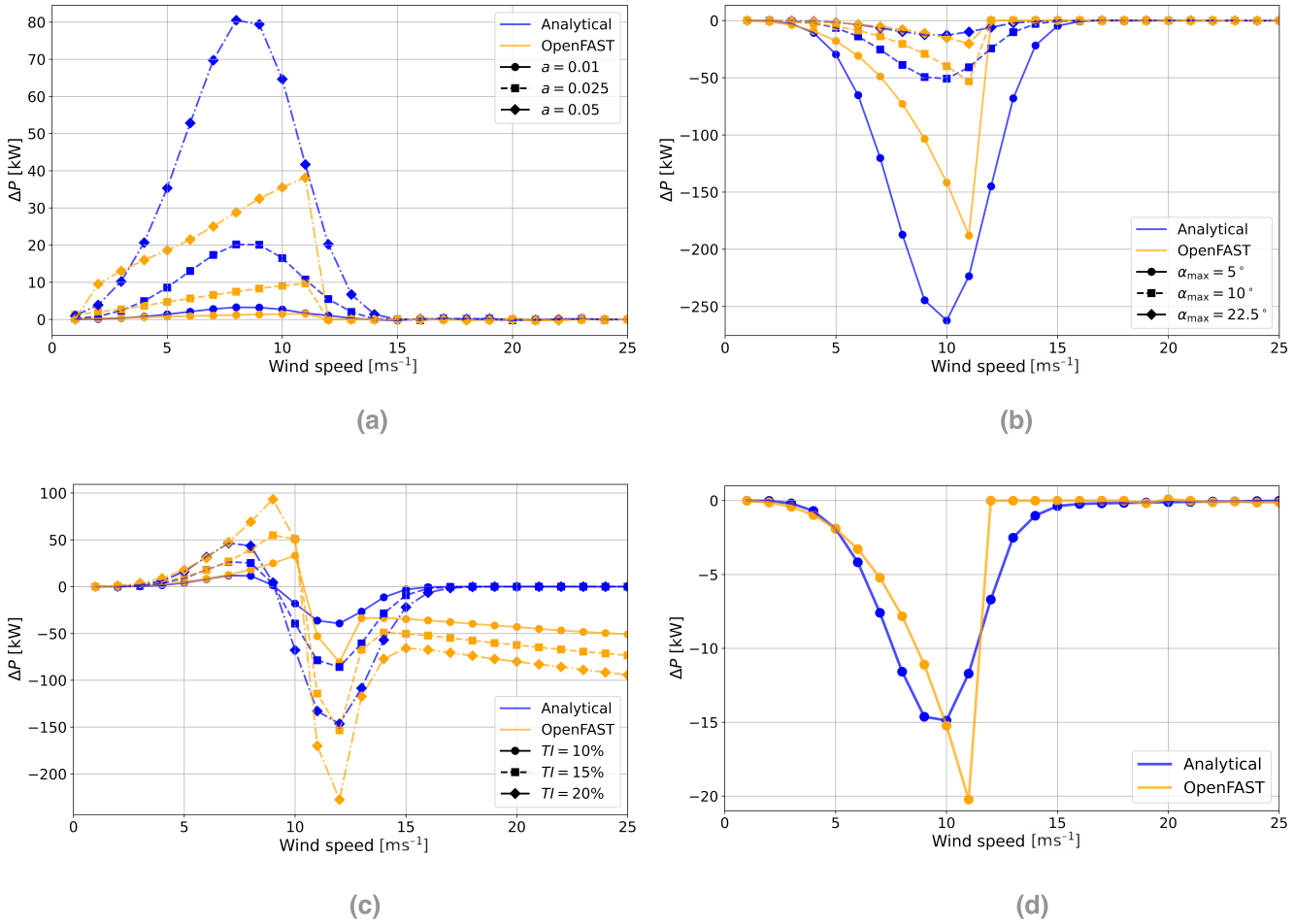


Figure 6. The difference in power production from a a uniform wind profile for the four idealised vertical wind profiles. (a) Linear shear, (b) Linear veer, (c) Homogeneous turbulence intensity (TI), and (d) Logarithmic wind profile ($z_0 = 0.1\,\mathrm{m}$).

4.1.1 Differences in power curves

The analytical model is parameterised using the power curve of the Enercon E92 2.35 MW turbines installed at the Gotthard Wind Park. The tabulated manufacturer power-curve data are fitted with the analytical expression introduced in Eq. 8, resulting in a smooth representation of $P(v)$ and its associated power coefficient $C_p(v)$, as shown in Fig. 7a.

The OpenFAST simulations, however, cannot be performed with the Enercon E92 directly, because a complete open aeroelastic model of this turbine is not available. The numerical simulations therefore use the open-source WindPACT 3.0 MW

reference turbine. This difference in turbine representation affects all comparisons between the analytical model and OpenFAST, because the two turbines do not share the same power curve, controller behaviour, or aerodynamic response. In particular, the WindPACT power curve exhibits features that are not representative of a modern commercial turbine power curve. Its $C_p(v)$ reaches unrealistically high values before remaining nearly constant until rated power is reached, and the model does not include clearly defined cut-in and cut-out wind speeds. As a result, the WindPACT turbine can produce power under wind conditions for which a real turbine would normally be curtailed or shut down, which may lead to an overestimation of energy production at low and high wind speeds.

A further distinction, that can be seen in Fig. 7, is that the two power curves represent different physical and methodological assumptions. The Enercon E92 power curve is based on long-term field measurements and therefore implicitly averages over a wide range of real atmospheric inflow conditions. By contrast, the WindPACT reference-turbine curve is derived for an idealised uniform inflow, where the wind speed is constant across the rotor plane. In reality, even a standard power-curve measurement includes some degree of vertical shear, veer, and turbulence, and could therefore be more closely represented by a logarithmic or power-law profile than by a perfectly uniform profile. Introducing such a correction would require an additional shear parameter, such as z_0 or α, but this information is not reported for the Enercon E92 power-curve calibration. Although it would be possible to estimate such a parameter from the test-site topography, the resulting value would remain uncertain because wind shear depends strongly on atmospheric stability, surface conditions, and wind direction (Bot, 2016; Emeis, 2005).

This distinction is also relevant for the interpretation of standardised power-curve measurements. The IEC 61400-12-1:2022 standard describes power-performance testing using nacelle-mounted measurements, including nacelle-mounted LiDAR systems that estimate the incoming wind field upstream of the turbine (IEC, 2022; Wagner et al., 2011). Commercial nacelle-mounted LiDARs often scan a conical pattern, so their measurements can include information from a finite region of the rotor-swept area rather than from a single point (Letizia et al., 2023; Rettenmeier et al., 2013). The resulting nacelle wind-speed signal is then calibrated against the turbine response and effectively converts a non-uniform, spatially variable inflow into a single representative wind-speed value. In this sense, the manufacturer power curve already contains an implicit averaging over realistic inflow variability, whereas the OpenFAST reference curve is tied more directly to the idealised uniform-inflow assumption.

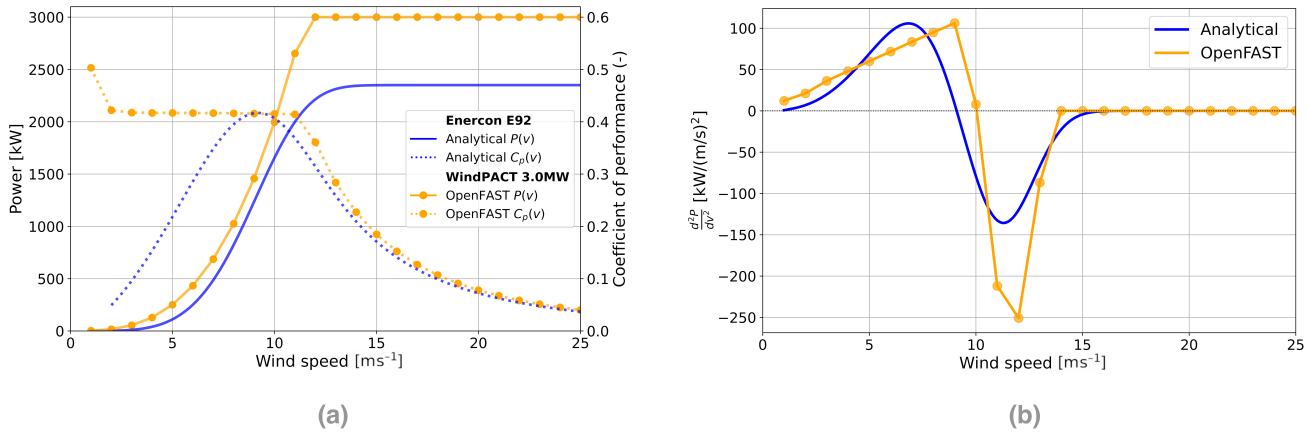


Figure 7. Comparison of the Enercon E92 2.35 MW and WindPACT 3.0 MW power curves, power coefficients, and curvature. (a) Power curves $P(v)$ and coefficients of performance $C_p(v)$, and (b) curvature of the power curves.

The second derivative of the power curve is shown in Fig. 7b. This curvature is central to the analytical framework, because it determines how wind-speed variations across the rotor-swept area affect mean power production. When different parts of the rotor experience different wind-speed regimes, the local curvature of $P(v)$ controls whether these variations increase or decrease the rotor-integrated power relative to a uniform inflow. The fitted Enercon E92 curve has a smooth curvature, whereas the WindPACT curve shows a nearly linear increase followed by an abrupt transition near rated power. These differences explain several of the features observed in the idealised-profile comparisons, including the more abrupt OpenFAST response and the smoother analytical response throughout the following results.

4.2 Gotthard wind profiles

We continue by evaluating the models under real-world conditions. For this purpose we have selected ten distinct wind events at each of the five turbines in the Gotthard Wind Park. Each case spans several hours and is classified by southerly or northerly flow (Tab. 2), which are the prevailing wind regimes for this mountain pass. For each event, we make use of the Gotthard Transect Experiment dataset (van Schaik et al., 2024), which includes ten Doppler wind LiDAR deployments along the pass, providing upwind vertical wind profiles from all five turbines and prevailing winds.

In Fig. 8, nine of the ten cases are shown; the case of Turbine 1 with LiDAR location 9 under southerly flow is omitted. The wake effects from Turbine 2 contaminating the LiDAR wind profiles before reaching Turbine 1 requires a separate case. This special case is discussed in Sec. 4.3.

The first sub-figure (Fig. 8a) compares the predicted and observed power output, with the turbulence module enabled for both models. As observed before in Fig. 6c, the turbulence improves power output until about $v = 10\ \mathrm{m\ s^{-1}}$, after which power

production is decreased, reducing deviation from the true power in all cases. Compared to the turbulence-free case (Fig. 8b), this model version achieves slightly better agreement with the measured power production which only becomes clear when considering the bias values in Tab. 2. Here, the analytical model clearly outperforms OpenFAST, which often overestimates power once the rated power of the turbine is reached. This behaviour can also be observed from the idealised wind profiles of Fig. 6.

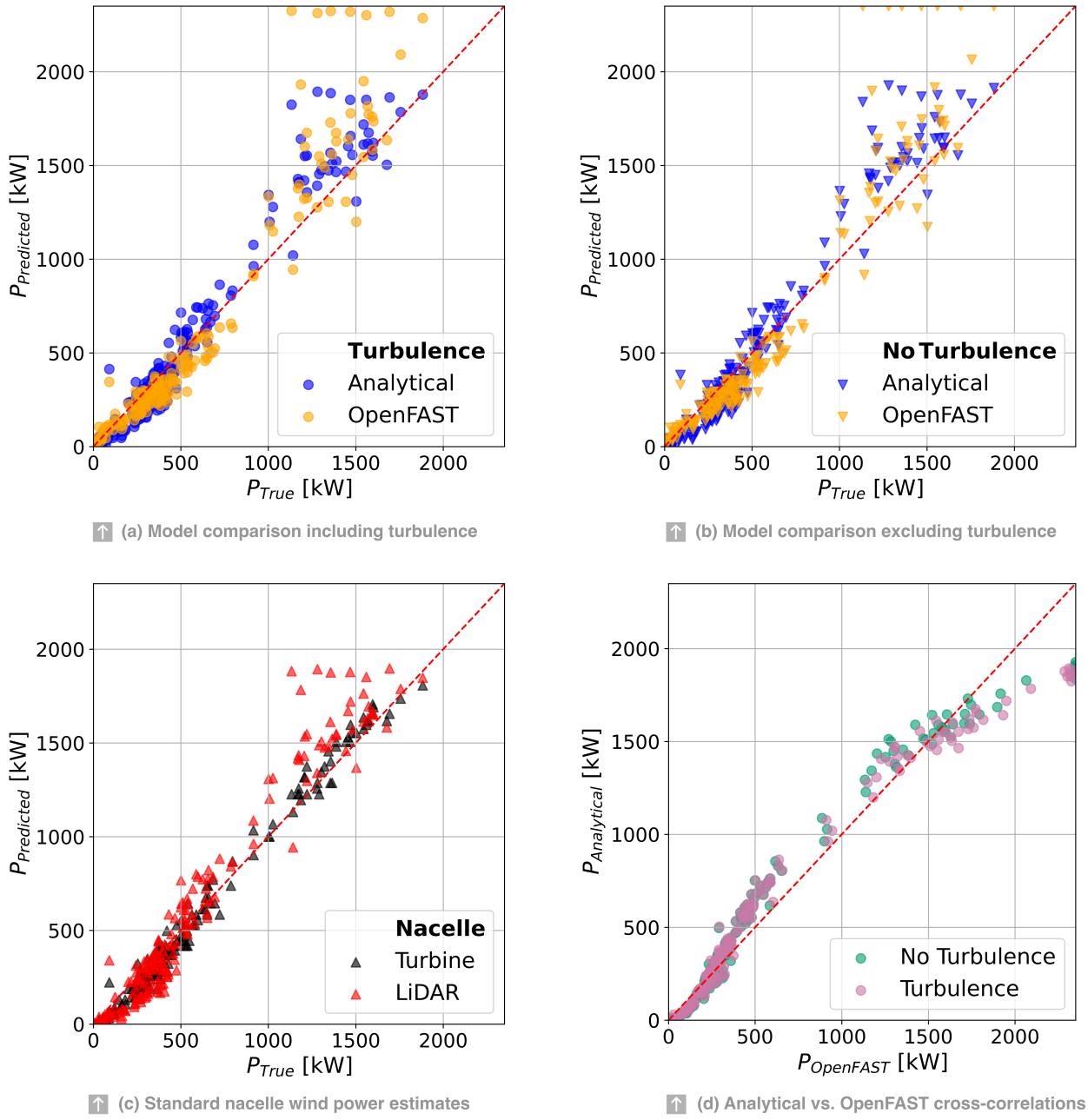


Figure 8. The differences in power production from the Analytical and OpenFAST models, and compared to standard approaches. (a) Comparison of the two models including turbulence and (b) excluding turbulence. (c) Standard nacelle power estimates from turbine anemometer and LiDAR and (d) Model cross-correlations.

In Fig. 8d, the cross-correlation between the analytical and OpenFAST models are shown. A systematic pattern can be observed here. Firstly, at low wind speeds, OpenFAST generates power earlier because it lacks a defined cut-in wind speed – a known unrealistic feature of the software. This should however not affect the results in a measurable way as the selected cases do not include the trivial case where $v < v_{in}$ where $P = 0\,\mathrm{kW}$. Secondly, in the intermediate region, the analytical model produces more power due to the stronger curvature of the power curve (Fig. 7b). Finally, at higher wind speeds, OpenFAST diverges again to greater power predictions, reflecting its unrealistic post-rated behaviour. Notably, the inclusion of turbulence only has a significant impact near rated power as the power curve flattens afterwards.

To connect these findings of the power prediction models to the IEC standard methods, the third sub-figure (Fig. 8c) shows predictions based on nacelle-height wind speed alone. The trivial case is the turbine nacelle measurement itself (black), which unsurprisingly correlates well with true power since it is effectively calibrated against it. Still, small deviations indicate the importance of vertical variations in the inflow. More striking is the performance of the LiDAR-based nacelle-height estimations (red), which effectively serve as the IEC-standard extrapolation method. In this case, we have data available at the nacelle-height, but the IEC standard only allows for measurements from up to two-thirds of hub-height to be extrapolated for this purpose. When considering the variety of the wind profiles measured by the LiDAR on the Gotthard pass, it becomes immediately evident that there is no single surface roughness that can be assigned to this site to perform such an extrapolation. We therefore remain at the best possible case for the IEC standard by taking the LiDAR range gate closest to the elevation of the nacelle. Relative to the IEC standard approach, the analytical model reports several improvements with the inclusion of the vertical wind profiles.

Table 2. Specification and error statistics of the ten Gotthard case study sites

Case study site			LiDAR–turbine	Number of	Bias from measured power [kW]			
Turbine	LiDAR	Wind direction	distance	wind profiles	Analytical	An. no-turb.	OpenFAST	IEC standard
T1	L9	Northerly	207 m	25	-14	-26	-50	-26
T1	L9	Southerly		25	-243*	-268*	-469	-556
T2	L5	Northerly	278 m	25	224	257	412	255
T2	L6	Southerly		25	-21	-25	-11	-26
T3	L10	Northerly	116 m	6	-33	-46	-80	-56
T3	L10	Southerly		25	-28	-37	17	-39
T4	L4	Northerly	156 m	25	131	158	155	142
T4	L4	Southerly		25	-13	-26	-54	-20
T5	L7	Northerly	114 m	25	68	65	-87	103
T5	L7	Southerly		25	-106	-122	-72	-134
				RMSE [kW]	140.3	150.5	215.7	153.8
				MAE [kW]	95.0	103.5	121.0	108.1
				R^2	0.911	0.897	0.794	0.893

* Corrected for wake effects

As shown in Tab. 2, the wind power bias reduction per site relative to the IEC standard ranges from 7.8 % to 46.4 %, depending on site complexity, with a mean bias reduction of 27.2 ± 12.3 %. The bias reduction is computed as the relative difference between the analytical approach and the IEC standard, defined as $(\text{Analytical} - \text{IEC})/\text{IEC}$, using the corresponding bias values from the first and last column of the Bias section of Tab. 2, excluding the T1-L9-Southerly (due to wake effects). The minimum and mean values are calculated as percentages based on the minimum and mean of this ratio. This improvement directly translates to a more accurate prediction of turbine power production: the analytical model yields production estimates that are on average 5.4 ± 3.8 % closer to observed values. Across the sites, this corresponds to improvements ranging from 0.9 % to 14.1 %. For the Gotthard Pass Enercon E-92 turbines, this equates to an average of 23.7 MWh per turbine closer to the true annual energy production. In terms of statistical error metrics, the analytical model reduces the RMSE by 8.8 %, and the MAE by 12.2 % compared to the IEC standard. However, the OpenFAST power predictions are consistently worse than the LiDAR nacelle-height wind speed method. This discrepancy can be primarily attributed to the different wind turbine used in the simulations, as the proprietary aerodynamic specifications of the Enercon E92 prevent its implementation in OpenFAST. Instead, the open-source WindPACT 3.0 MW turbine had to be employed and scaled, introducing systematic differences that affect the comparability of results.

In these OpenFAST simulations of the Gotthard wind profiles, the *USRVKM* turbulence mode in TurbSim was used, providing vertical turbulence variations and the ability to specify eddy length scales, unlike the IEC Kaimal spectrum mode used for the idealised profiles. Sensitivity tests across a range of turbulence intensities and eddy scales showed only minor effects on

power predictions, primarily at high wind speeds. Given that the analytical model already demonstrates superior performance, the standard *USRVKM* settings were retained.

Overall, the results show that while nacelle-height extrapolation can provide reasonable fits, the analytical model generalises significantly better for complex terrain site assessments. Including turbulence further sharpens its predictive skill, particularly at high wind speeds, while retaining negligible computational cost compared to OpenFAST.

4.3 Wake filtering

In Fig. 9a, the original LiDAR wind measurements from LiDAR location 9 for southerly wind conditions, relative to Turbine 1, are shown in orange, together with a subset of points selected outside the wake-contaminated region. From the analysis of wake direction and extent, this case was identified as the only instance where either the LiDAR or the turbine is affected by a wake. Specifically, for Turbine 1 and LiDAR location 9 under southerly wind conditions, the wake from Turbine 2 intersects the LiDAR beam but consistently bypasses Turbine 1. This becomes evident when considering the turbine position angle of Turbine 2: extending a line downstream on the lee side of the turbine, while accounting for the swept area of the rotor, shows that the wake passes over LiDAR location 9 but does not intersect Turbine 1. As a result, the LiDAR profile misrepresents the true inflow conditions of the turbine.

The error bars of both the orange and green profiles, as well as the shaded blue region, represent the standard deviation of the wind speed, during the 10 min time window in which complete wind profiles are measured every 5 seconds. After wake filtering, the resulting profile (blue) behaves much more consistently as if no wake was present, which is also observed by the reduced turbulence intensity, also interpolated by the Taylor expansion.

The effect on power predictions due to the filtering of the wake is shown in Fig. 9b. The unfiltered case, with analytical and OpenFAST predictions in blue and orange respectively, substantially underestimates the measured turbine power. After applying the wake filter, the analytical results align much more closely with the actual turbine production. Quantitatively, the RMSE decreases from 515.8 kW to 242.9 kW, which is a reduction of 53 %, while the bias is reduced by 58 % to -215.3 kW. The only trade-off is a slight decrease in correlation, from 0.55 to 0.50, indicating that the effectiveness of the wake correction varies between individual profiles. This is to be expected as the procedure simply removes a standard range of wind measurements where the wake is expected based on the height of the swept area of Turbine 2 with respect to the elevation of the LiDAR. In some cases, particularly when the wind field contains a vertical component, wake remnants may still contaminate the higher points, or the correction may overcompensate, as visible in one outlier above the $1:1$ line.

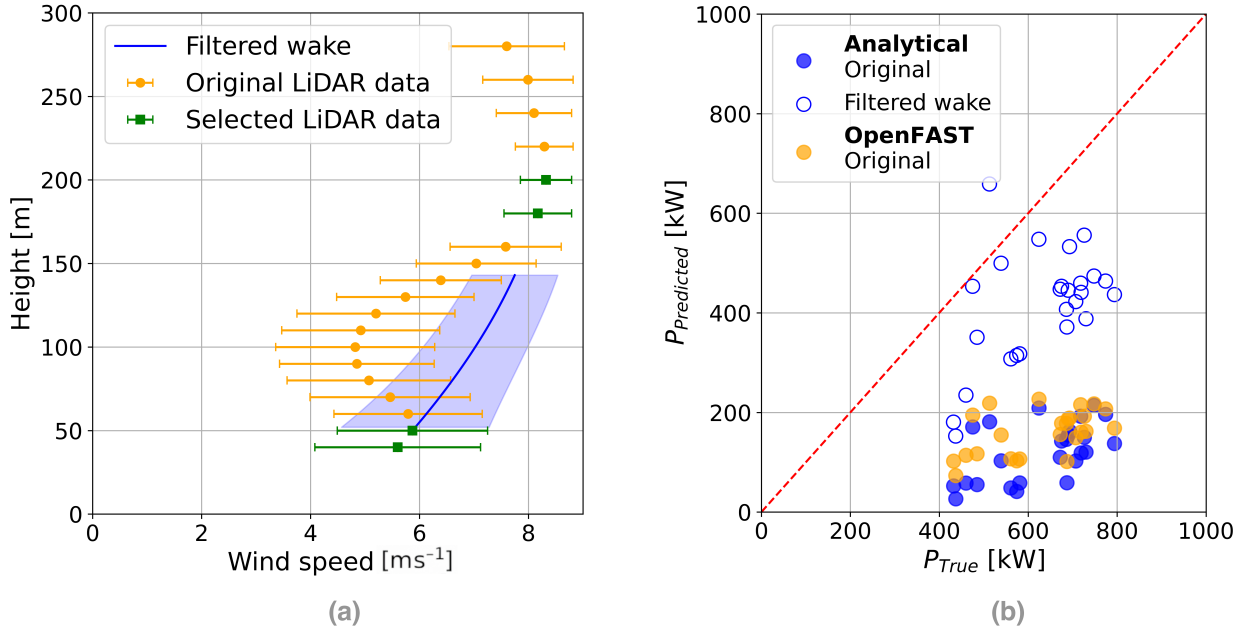


Figure 9. Wake filtering of LiDAR location 9 with Turbine 1 under Southerly winds (a) wind profile and (b) power production comparison.

Despite these limitations, the approach works remarkably well and highlights a key advantage of the analytical model: it can be applied flexibly to almost any kind of input data. Whether only two measurement levels are available or a densely resolved LiDAR profile, the Taylor expansion method adapts naturally. This stands in stark contrast to the OpenFAST method which cannot directly accommodate such filtering. Importantly, the method is also turbine-independent: even before a specific turbine type is selected, a single LiDAR deployment can provide accurate wind energy assessments for any size turbine. Furthermore, wake-filtered profiles can be particularly valuable in cases such as wind farm expansions, where wake contamination is unavoidable, yet filtering offers a practical way to recover representative inflow profiles such as in off-shore applications where one can expect the unaffected wind profile to be similar within a few kilometres from the LiDAR site.

4.4 Robustness and sensitivity tests

In addition to the core results, several supplementary tests were conducted to evaluate the robustness of the analytical model. First, the shaft tilt was tested. In the main numerical simulations, the shaft tilt is set to 0° to remain consistent with the analytical formulation. A more realistic value of 5°, as reported in the Enercon E92 technical specifications, introduces a small bias of approximately 8 kW for the 2.35 MW turbine. However, since the wind profile is based on a LiDAR measurement located roughly 100 m from the turbine, any slight decrease in horizontal inflow or inclusion of vertical wind components caused by shaft tilt would not necessarily improve the accuracy of the comparison. The simpler 0° configuration is therefore retained, as it is more directly comparable to the idealised wind-profile experiments.

Secondly, the sensitivity to air density was investigated using OpenFAST simulations across a range of values representative of wind parks at different elevations. The analytical model remains well behaved across the full range, with no need to adjust the shape of the $C_p(v)$ curve. This confirms that the formulation can be transferred to sites at different elevations, provided that the air-density dependence of available wind power is treated consistently.

Thirdly, the influence of turbulent integral length scale and component scaling was evaluated. As described in App. B, the original USRVKM settings use a short example length-scale profile of $L = [3, 4, 6, 9, 13, 13, 13, \ldots]\ \mathrm{m}$ and component scaling $(1.092, 1.000, 0.534)$. These settings are not interpreted as physically representative atmospheric length scales for the Gotthard Pass. Effective length scales estimated from the 1 Hz LiDAR data are substantially larger, with median streamwise values of approximately 50–$70\ \mathrm{m}$ over the measured height range. However, the individual 10-minute estimates show large variability, ranging from a few metres to several hundred metres depending on height, component, and inflow period. The standard deviations of the height-dependent estimates are of order 70–100 m, which is comparable to, or larger than, the variation of the median profile itself.

This large spread indicates that there is no single objectively correct turbulent length-scale profile for all simulated cases. A case-specific prescription of $L_u(z)$, $L_v(z)$, and $L_w(z)$ for each individual OpenFAST inflow period would introduce an additional, poorly constrained degree of freedom and would shift the focus of the study towards turbulence parameterisation in TurbSim. Similarly, the component scaling is not uniquely constrained: the LiDAR-derived scaling is $(1.00, 1.04, 1.20)$ with robust uncertainty margins of approximately $(0.00, 0.10, 0.26)$, while generic onshore values such as $(1.0, 0.8, 0.6)$ represent broader empirical assumptions rather than site-specific measurements. We therefore treat both the length-scale profile and the component scaling as sensitivity parameters rather than as uniquely measurable constants.

To test whether this uncertainty affects the main conclusions, a representative subset of turbulent OpenFAST simulations was repeated using alternative length-scale and component-scaling settings. The tested configurations include the original short-scale USRVKM example profile, a modified component scaling of $(1.0, 0.8, 0.6)$, a length-scale profile increased by a factor of ten, and a combined case in which both modifications are applied. These configurations were selected to span the largest deviations considered in the velocity-spectrum comparison and therefore provide a conservative sensitivity test. For each configuration, six turbulent realisations were simulated using different random seeds. The ensemble-mean 10-minute power changes only marginally between the cases: from $1151\ \mathrm{kW}$ in the base case to $1151\ \mathrm{kW}$ for the modified component scaling, $1151\ \mathrm{kW}$ for the increased length scales, and $1150\ \mathrm{kW}$ when both modifications are applied. Relative to the base case, these differences are -0.02%, -0.07%, and -0.11%, respectively, corresponding to changes of only about 0.2–$1.3\ \mathrm{kW}$.

The main effect of the modified turbulence settings is therefore not a systematic shift in mean power, but a modest increase in realisation-to-realisation variability. To assess the influence of the stochastic turbulence realisation, the sensitivity simulations were repeated using six different TurbSim random seeds. This was done for the representative case in which the largest deviations in the velocity spectra were observed, corresponding to wind profiles around $9\ \mathrm{m\ s^{-1}}$. The aim of this test is not to form a full six-seed ensemble for every OpenFAST inflow period, but to quantify whether the conclusions are sensitive to the random realisation in a conservative case.

The resulting seed-to-seed variability is small compared with the systematic model differences discussed in the main comparison. The standard deviation of the 10-minute mean power across the six realisations is approximately 1 kW for the base configuration and for the isolated component-scaling modification, and increases to approximately 4 kW when the length-scale profile is increased by a factor of ten. Even this larger spread corresponds to only about 2 % of the mean OpenFAST bias of approximately 200 kW. The ensemble mean also changes by only about 0.2–1.3 kW between the tested turbulence configurations. This indicates that the random turbulence seed affects individual OpenFAST realisations only weakly in terms of 10-minute mean power. A full six-seed ensemble for every inflow case would therefore substantially increase the computational cost without changing the conclusions of the comparison.

Fourthly, we tested the impact of using alternative turbine power curves. When replacing the Enercon E92 curve with the WindPACT 3.0 MW reference-turbine curve, the agreement between the analytical model and OpenFAST becomes closer, although this improvement is primarily due to a degradation of the analytical model rather than an enhancement of OpenFAST. This illustrates that the framework can be applied to arbitrary power curves, as the analytical approximation in Eq. 8 is flexible and well behaved.

Finally, we assessed the impact of temporal averaging on estimates of $\overline{v^3}$ by aggregating the 1 s LiDAR wind-speed data over a range of averaging intervals: 1, 2, 5, 10, 20, and 30 minutes, and 1 hour. Changing the averaging window slightly modifies the resulting wind profiles, which in turn affects the analytically derived power production. These differences remain relatively small, on the order of 4 % (in the order of 3 kW for the 3 MW turbine at $TI = 15$ %). While this effect is not explored further, it is noted as a minor source of uncertainty. In line with standard wind-energy practice, 10-minute averages are adopted throughout this study.

Together, these tests demonstrate that the analytical model is robust to variations in shaft tilt, air density, turbine power curve, temporal averaging, and the order of magnitude of the turbulent length-scale assumptions used in OpenFAST. The turbulent length-scale sensitivity confirms that the originally used short USRVKM profile should not be interpreted physically, but also shows that replacing it by a single alternative profile does not define a unique "correct" turbulence field. Instead, the LiDAR-derived length scales provide a physically motivated sensitivity range, within which the main mean-power conclusions of the analytical model remain unchanged.

5 Conclusions

In this study, we introduced and validated a new analytical framework for predicting wind turbine power production that explicitly accounts for vertical wind profile variability through an integral formulation. By combining Taylor expansions of the inflow with an analytical representation of the turbine power curve, the model provides a clearly improved alternative to the IEC standard for wind energy assessment based on a single nacelle-height wind measurement. Furthermore, it provides a flexible alternative to costly numerical simulation of wind turbine aerodynamics.

The results show that the primary discrepancies between the analytical model and OpenFAST can be attributed to differences in the turbine power curves. While the analytical model was configured for the Enercon E-92 turbine, reflecting the real-world

LiDAR measurements at the Gotthard Pass, OpenFAST required the use of the WindPACT 3.0 MW reference turbine. The unusual $C_p(v)$ curve of the latter, including the absence of realistic cut-in and cut-out wind speeds, amplified differences in the response to vertical wind profile variations. This effect is best represented by considering the curvature ($\frac{d^2P}{dv^2}$) of the power curve, which confirms the mechanism and provided an explanation for the observed discrepancies in the predicted power of the turbines.

When applying the analytical model to idealised wind profiles, such as linear shear, linear veer, logarithmic wind profiles, as well as homogeneous turbulence intensities, we demonstrated that the analytical formulation produces smoother and more physically consistent power predictions compared to OpenFAST. These differences are likely driven by the different power curves.

This same effect is also visible in the real Gotthard LiDAR profiles, which provided a direct validation against real-world inflow conditions. The vertical wind profiles at this alpine site are strongly shaped by shear, veer, and turbulence, and represent a complex but highly relevant test case for wind energy production. Compared to OpenFAST, the analytical model showed smoother and more consistent responses to these profiles, reflecting the more regular curvature of the Enercon E-92 power curve used in its formulation. Resulting in remarkably high goodness of fit of $R^2 = 0.911$, with typical bias reduction of 27.2 ± 12.3 % which corresponds to an annual average of 23.7 MWh per turbine (Enercon E92 2.35 MW) closer to the true production power for this highly complex Alpine site.

The wake filtering analysis further illustrated the strength of the analytical approach by means of its flexibility: By excluding the portion of the LiDAR profile affected by a turbine wake, the analytical model predictions were brought significantly closer to the measured power, reducing the RMSE and Bias by more than 50 %, significantly closer to the typical skill of the other cases. Although, the slight decrease in correlation suggests that this method does not work as effectively on ewind profile due to leaking over wake effects. Further work should consult the plethora of literature available on wake detection, which will likely be the remedy to this rather straight-forward problem that is outside of the scope of this work.

Further robustness and sensitivity tests confirmed that the analytical framework performs consistently across a range of air densities representative of all elevations, and that the method can be applied to arbitrary power curves thanks to the analytical approximation of Eq. 8. Sensitivity tests with lidar-derived turbulent length scales further show that the exact TurbSim eddy-scale parameterisation mainly affects the stochastic OpenFAST realisations, while the 10-minute mean-power conclusions remain robust within the tested range. Furthermore, we have conducted tests on the sensitivity of the 10-minute averaging window which has become state-of-the-art in the wind energy industry and conclude that this does introduce a small additional, and probably unavoidable, uncertainty of up to 4 % in the power prediction. This effect is minor and not of interest to study further given the trade-off with turbulence statistics.

In summary, the analytical model developed here applies a simple physical interpretation of vertical variations in the wind in a computationally efficient and highly flexible tool for assessing turbine power production under vertically varying wind conditions. It captures the essential mechanisms behind power output variations, explains discrepancies with simulation-based models through power curve curvature, and can be robustly applied across sites, turbines and measurement configurations. Beyond its application in the Swiss Alps with the Gotthard Pass case study, the model offers a new pathway to bridge measure-

ments that we think should be considered to be amended in today's wind energy assessment standards, as it is low impact due to our open-source code for the tool, and the trend of using LiDAR in site selection for wind parks which already include this additional information of vertical wind profiles. We particularly want to highlight the value in the practicality of use in the majority of cases where wind turbine aerodynamic specifications are proprietary. Something that more sophisticated simulations and other state-of-the-art tools require, which is completely avoidable by this method.

Appendix A: Analytical power equation derivation

From Taylor series theory, a continuous function such as the wind speed profile can be approximated by a polynomial:

$$v(z) = \sum_{i=0}^{N} c_i z^i \tag{A1}$$

The standard turbine power equation is:

$$P(z) = \frac{1}{2} C_p(v) \rho A v(z)^3 \tag{A2}$$

We integrate over the circular swept area by converting the surface integral to a 1D integral in height:

$$P = \frac{1}{2} C_p(v) \rho \int_{-R}^{R} 2\sqrt{R^2 - z^2}\, v(z)^3 \, \mathrm{d}z \tag{A3}$$

To integrate over the height z, we must define the cube of the wind speed that is parallel to the normal vector of the swept area:

$$(v(z))^3 = \sum_{i,j,k=0}^{N} c_i c_j c_k z^{i+j+k} = \sum_{i=0}^{N} \left(c_i \sum_{j=0}^{N} \left(c_j \sum_{k=0}^{N} \left(c_k z^{i+j+k} \right) \right) \right) \tag{A4}$$

We solve this analytically by the following subtitution:

$$z = R\sin(u), u = \arcsin\left(\frac{z}{R}\right), dz = R\cos(u)du \tag{A5}$$

Such that the power equation becomes:

$$P(v,u) = \frac{1}{2} C_p(v) \rho \int_{\frac{-\pi}{2}}^{\frac{\pi}{2}} 2R\cos(u)\sqrt{R^2 - R^2\sin^2(u)} \sum_{i,j,k=0}^{N} c_i c_j c_k R^{i+j+k} \sin^{i+j+k}(u) \mathrm{d}u \tag{A6}$$

Simplifying by removing the factor 2 out of the integral, and by rearranging the square root:

$$P(v,u) = C_p(v) \rho \int_{\frac{-\pi}{2}}^{\frac{\pi}{2}} R\cos(u)\sqrt{R^2(1 - \sin^2(u))} \sum_{i,j,k=0}^{N} c_i c_j c_k R^{i+j+k} \sin^{i+j+k}(u) \mathrm{d}u \tag{A7}$$

The square root can be resolved by a trigonometric substitution to find:

$$P(v,u) = C_p(v)\rho \int_{\frac{-\pi}{2}}^{\frac{\pi}{2}} R^2 \cos^2(u) \sum_{i,j,k=0}^{N} c_i c_j c_k R^{i+j+k} \sin^{i+j+k}(u) \mathrm{d}u \tag{A8}$$

We can move the triple summation, including several constants out of the integral to simplify the integral to a purely trigonometric problem:

$$P(v,u) = C_p(v)\rho R^2 \sum_{i,j,k=0}^{N} c_i c_j c_k R^{i+j+k} \int_{\frac{-\pi}{2}}^{\frac{\pi}{2}} \cos^2(u) \sin^{i+j+k}(u) \mathrm{d}u \tag{A9}$$

We now focus on the integral only, by defining it as Q_m:

$$P(v,u) = C_p(v)\rho R^2 \sum_{i,j,k=0}^{N} c_i c_j c_k R^{i+j+k} Q_m(u) \tag{A10}$$

Where the substitution $Q(z)$ also replaces $i+j+k$ by a new integer m:

$$Q_m(u) = \int_{\frac{-\pi}{2}}^{\frac{\pi}{2}} \cos^2(u) \sin^m(u) \mathrm{d}u, \, m = i+j+k \tag{A11}$$

For odd values of m, the integrand $\cos^2(u)\sin^m(u)$ is an odd function, and the integral over the symmetric interval $[-\pi/2, \pi/2]$ evaluates to 0:

$$Q_m(u) = 0, \quad \text{if } m \text{ is odd.} \tag{A12}$$

For even values of m, let $m = 2s$, where s is an integer. The integrand $\cos^2(u)\sin^{2s}(u)$ an even function, and by symmetry, the integral can be simplified by doubling the range from $[0, \pi/2]$:

$$Q_m(u) = 2\int_{0}^{\frac{\pi}{2}} \cos^2(u) \sin^{2s}(u) \, \mathrm{d}u, \quad \text{if } m = 2s. \tag{A13}$$

We once again apply the trigonometric identity to eliminate the cosine from the integrand.

$$Q_m(u) = 2\int_{0}^{\frac{\pi}{2}} \left(1 - \sin^2(u)\right) \sin^{2s}(u) \mathrm{d}u, \quad \text{if } m = 2s. \tag{A14}$$

Using $1 - \sin^2(u) = \cos^2(u)$, this becomes:

$$Q_m(u) = 2\int_{0}^{\frac{\pi}{2}} \sin^{2s}(u) \cos^2(u) \, \mathrm{d}u. \tag{A15}$$

This integral directly corresponds to the Beta function, yielding:

$$Q_m(u) = B\left(s + \frac{1}{2}, \frac{3}{2}\right). \tag{A16}$$

where $B(x, y)$ is the Beta function, defined as $B(x, y) = \frac{\Gamma(x)\Gamma(y)}{\Gamma(x+y)}$.

Such that $Q_m(u)$, for even values of $m = 2s$, is given by:

$$Q_m(u) = \sqrt{\pi}\left(\frac{\Gamma\left(s+\frac{1}{2}\right)}{\Gamma(s+1)} - \frac{\Gamma\left(s+\frac{3}{2}\right)}{\Gamma(s+2)}\right) \tag{A17}$$

And the turbine power equation is given by:

$$P(v) = C_p(v)\rho R^2 \sum_{i,j,k=0}^{N} c_i c_j c_k R^m \sqrt{\pi}\left(\frac{\Gamma\left(s+\frac{1}{2}\right)}{\Gamma(s+1)} - \frac{\Gamma\left(s+\frac{3}{2}\right)}{\Gamma(s+2)}\right) \quad m = 2s = i+j+k \,|\, m \text{ is even} \tag{A18}$$

Which is only a function of wind speed v again.

The Gamma function $\Gamma(x)$, is defined by:

$$\Gamma(x) = \int_0^\infty t^{z-1} e^{-t}\,\mathrm{d}t \tag{A19}$$

For positive integers, where $x = s = m/2 = (i+j+k)/2$ (with m the sum of the three positive integers), the Gamma function simplifies as:

$$\Gamma(m) = (m-1)! \tag{A20}$$

To evaluate the Gamma function at half-integer values, consider $z = m + \frac{1}{2}$, where m is a non-negative integer. The key idea comes from using the recursive property of the Gamma function and its relationship with the factorial for half-integer arguments.

Using the reflection formula and the recurrence relation:

$$\Gamma\left(\frac{1}{2}\right) = \sqrt{\pi} \tag{A21}$$

and for higher half-integer values, you apply the recurrence relation $\Gamma(z+1) = z\Gamma(z)$ repeatedly. The general result for half-integer values of $\Gamma\left(n + \frac{1}{2}\right)$ (where n is a non-negative integer) is:

$$\Gamma\left(s + \frac{1}{2}\right) = \frac{(2s)!}{4^s s!}\sqrt{\pi} \tag{A22}$$

Thus, the Gamma function evaluated at half-integers $s+\frac{1}{2}$ is a product of a factorial expression, $\sqrt{\pi}$, and powers of 4.

Such that finally we can replace the full integer Gamma functions

$$P(v) = C_p(v)\rho\sqrt{\pi}R^2 \sum_{i,j,k=0}^{N} c_i c_j c_k R^m \left(\frac{\Gamma(s+\frac{1}{2})}{s!} - \frac{\Gamma(s+\frac{3}{2})}{(s+1)!} \right), \quad m = 2s = i+j+k \,|\, m \text{ is even} \tag{A23}$$

We apply the recurrence relation on the $\Gamma(s+\frac{3}{2})$:

$$P(v) = C_p(v)\rho\sqrt{\pi}R^2 \sum_{i,j,k=0}^{N} c_i c_j c_k R^m \left(\frac{\Gamma(s+\frac{1}{2})}{s!} - \frac{\left(s+\frac{1}{2}\right)\Gamma(s+\frac{1}{2})}{(s+1)!} \right), \quad m = 2s = i+j+k \,|\, m \text{ is even} \tag{A24}$$

We rearrange to a single Gamma function:

$$P(v) = C_p(v)\rho\sqrt{\pi}R^2 \sum_{i,j,k=0}^{N} c_i c_j c_k R^m \left(\frac{(s+1)! - s!(s+\frac{1}{2})}{s!(s+1)!} \Gamma\left(s+\frac{1}{2}\right) \right), \quad m = 2s = i+j+k \,|\, m \text{ is even} \tag{A25}$$

Reduce the $(s+1)!$ to $s!(s+1)$:

$$P(v) = C_p(v)\rho\sqrt{\pi}R^2 \sum_{i,j,k=0}^{N} c_i c_j c_k R^m \left(\frac{s!(s+1) - s!(s+\frac{1}{2})}{s!(s+1)!} \Gamma\left(s+\frac{1}{2}\right) \right), \quad m = 2s = i+j+k \,|\, m \text{ is even} \tag{A26}$$

Which cancels out the $s!$:

$$P(v) = C_p(v)\rho\sqrt{\pi}R^2 \sum_{i,j,k=0}^{N} c_i c_j c_k R^m \left(\frac{1}{2}\frac{1}{(s+1)!} \Gamma\left(s+\frac{1}{2}\right) \right), \quad m = 2s = i+j+k \,|\, m \text{ is even} \tag{A27}$$

We finally use the general result for half-integer values of the Gamma function to find:

$$P(v) = C_p(v)\rho\pi R^2 \sum_{i,j,k=0}^{N} c_i c_j c_k R^m \frac{1}{2}\frac{1}{(s+1)!}\frac{(2s)!}{4^s s!}, \quad m = 2s = i+j+k \,|\, m \text{ is even} \tag{A28}$$

Where the $\sqrt{\pi}$ reunites with the other $\sqrt{\pi}$ to arrange $A = \pi R^2$ which obviously refers to the swept area of the blade A. We also replace s with $m/2$:

$$P(v) = C_p(v)\rho\pi R^2 \sum_{i,j,k=0}^{N} c_i c_j c_k R^m \frac{1}{2}\frac{1}{(\frac{m}{2}+1)!}\frac{m!}{2^m \frac{m}{2}!}, \quad m = i+j+k \,|\, m \text{ is even} \tag{A29}$$

Some final mathematical book-keeping where the half is moved to the front and πR^2 is combined to reflect the regular expression of the power equation, and by rearranging the factorials and exponents of 2, results in

$$\boxed{P(v) = \frac{1}{2}C_p(v)\rho A \sum_{i,j,k=0}^{N} c_i c_j c_k R^m \frac{m!}{2^m(\frac{m}{2}!)^2(\frac{m}{2}+1)}, \quad m = i+j+k \,|\, m \text{ is even}} \tag{A30}$$

Which brings us back to the familiar structure of the turbine power Eq. 2.

Proving that there exists a general analytical solution for the turbine power output for any continuous function $v(h)$ as an inflow of a wind turbine.

This large fraction of factorials, is separated for readability and defined as K_m, and only has to be calculated for even values of m and can be found for $m \leq 10$ in Tab. A1:

$$K_m = \frac{m!}{2^m \left(\frac{m}{2}!\right)^2 \left(\frac{m}{2}+1\right)}, \quad m = i+j+k \,|\, m \text{ is even} \tag{A31}$$

Table A1. Look-up table for values of m for the large factorial fraction K_m.

m	fraction
0	1
2	$\frac{1}{4}$
4	$\frac{1}{8}$
6	$\frac{5}{64}$
8	$\frac{7}{128}$
10	$\frac{21}{512}$

A1 Verification: units

As verification of this derivation, we can check the units of this equation:

$$P \rightarrow \left[\mathrm{W} = \mathrm{N\,m\,s^{-1}} = \mathrm{kg\,m^2\,s^{-3}}\right], \tag{A1}$$

$$C_p \rightarrow [1], \tag{A2}$$

$$\rho \rightarrow \left[\mathrm{kg\,m^{-3}}\right], \tag{A3}$$

$$R^2 \rightarrow \left[m^2\right], \tag{A4}$$

$$c_i, c_j, c_k \rightarrow \left[\mathrm{m^{1-i}s^{-1}}\right], \left[\mathrm{m^{1-j}s^{-1}}\right], \left[\mathrm{m^{1-k}s^{-1}}\right], \tag{A5}$$

$$R^{i+j+k} \rightarrow \left[\mathrm{m^{i+j+k}}\right]. \tag{A6}$$

Such that:

$$\left[\mathrm{kg\,m^2\,s^{-3}}\right] = [1] \cdot \left[\mathrm{kg\,m^{-3}}\right] \cdot \left[\mathrm{m^2}\right] \cdot \left[\mathrm{m^{1-i}s^{-1}}\right] \cdot \left[\mathrm{m^{1-j}s^{-1}}\right] \cdot \left[\mathrm{m^{1-k}s^{-1}}\right] \cdot \left[\mathrm{m^{i+j+k}}\right] \tag{A7}$$

Which indeed agrees.

A2 Verification: linear shear

Additionally, we can verify whether this is correct by taking a linear equation for $v(z) = v_0 + az = c_0 + c_1 z$, such that $N = 1$. Starting from Eq. 4, we insert $v(z)^3 = (c_0 + c_1 z)^3$ and expand:

$$v(z)^3 = c_0^3 + 3c_0^2 c_1 z + 3c_0 c_1^2 z^2 + c_1^3 z^3. \tag{A8}$$

Due to symmetry of the integral over $[-R, R]$, the odd terms vanish, such that only the z^0 and z^2 terms remain. Using the standard integrals over the rotor disk then yields:

$$P(v) = \frac{1}{2} C_p(v) \rho A \left(c_0^3 + 3c_0 c_1^2 R^2 \cdot \frac{1}{4} \right) = \frac{1}{2} C_p(v) \rho A \left(v_0^3 + \frac{3}{4} R^2 a^2 v_0 \right) \tag{A9}$$

Which agrees with regular integration of this function.

A3 Verification: linear veer

Similarly, let us verify the veer equation $v(z) = \overline{v}\cos(\alpha_{max}\frac{z}{R})$ by Taylor expansion to the second order:

$$v(z) \approx \overline{v} - \frac{\overline{v}\alpha_{\max}^2}{2R^2}z^2 = c_0 + c_2 z^2 \tag{A10}$$

with $c_0 = \overline{v}$, $c_1 = 0$, and $c_2 = \overline{v}\frac{\alpha_{\max}^2}{2R^2}$, where the z^4 and higher terms are discarded. Expanding $v(z)^3$ gives:

$$v(z)^3 = c_0^3 + 3c_0^2c_2z^2 + 3c_0c_2^2z^4 + c_2^3z^6. \tag{A11}$$

Substituting into Eq. 4 and using the known integrals for $z^m\sqrt{R^2 - z^2}$ leads to:

$$P(v) = \frac{1}{2}C_p(v)\rho A\left(c_0^3 + 3c_0^2c_2R^2\cdot\frac{1}{4} + \cancel{3c_0c_2^2R^4\cdot\frac{1}{8} + c_2^3R^6\cdot\frac{5}{64}}\right) \approx \frac{1}{2}C_p(v)\rho A\overline{v}^3\left(1 - \frac{3}{8}\frac{\alpha_{\max}^2}{R^2}\right) \tag{A12}$$

Where we also discarded the R^4 and R^6 terms, which agrees again with the regular integration method.

Appendix B: Estimation of effective turbulent length scales from the LiDAR data

Effective turbulent length scales are estimated from the high-frequency WindCube LiDAR data to provide a physically motivated sensitivity case for the TurbSim inflow generation. The purpose of this analysis is not to derive a unique turbulence parameterisation for the Gotthard Pass, but to estimate the order of magnitude and vertical variation of the energy-containing eddies during the inflow periods used for the OpenFAST comparison.

The WindCube data consist of sequential line-of-sight radial velocities from the five beam positions $0°$, $90°$, $180°$, $270°$, and V. For each measurement height z, the radial velocities are first separated by beam position. The opposing $0°$ and $180°$ beams are sign-corrected and combined to form an effective streamwise, or common-wind, component $u(t, z)$. The opposing $90°$ and $270°$ beams are treated analogously to form an effective lateral component $v(t, z)$. The vertical beam V is used directly to form the vertical component $w(t, z)$. A carrier-to-noise-ratio threshold of -23 dB is applied before calculating the length scales.

For each selected OpenFAST inflow period, the component time series are divided into 10-minute windows. Within each window, the mean is removed from each component,

$$u_i'(t, z) = u_i(t, z) - \overline{u_i}(z), \tag{B1}$$

where $i \in \{u, v, w\}$. The normalised autocorrelation function is then calculated as

$$R_{ii}(\tau, z) = \frac{\overline{u_i'(t, z)u_i'(t + \tau, z)}}{\overline{u_i'^2(t, z)}}. \tag{B2}$$

The integral timescale is obtained by integrating the autocorrelation function up to its first zero crossing,

$$T_i(z) = \int_0^{\tau_0} R_{ii}(\tau, z)\,\mathrm{d}\tau, \tag{B3}$$

where τ_0 is the first lag for which $R_{ii}(\tau, z) \leq 0$. The corresponding effective integral length scale is then estimated using Taylor's frozen-turbulence hypothesis,

$$L_i(z) = \overline{U}(z) T_i(z), \tag{B4}$$

where $\overline{U}(z)$ is the mean reconstructed horizontal wind speed at the same height and within the same 10-minute window.

The final height-dependent base length scale used in the sensitivity analysis is defined from the streamwise component,

$$L(z) = \mathrm{median}\left[L_u(z)\right], \tag{B5}$$

where the median is taken over all valid 10-minute windows from the selected OpenFAST inflow periods. Robust uncertainty margins are calculated from the 16th–84th percentile range of the valid 10-minute estimates. The reported uncertainty corresponds to half of this range,

$$\Delta L(z) = \frac{P_{84}\left[L_u(z)\right] - P_{16}\left[L_u(z)\right]}{2}. \tag{B6}$$

This provides a robust measure of the spread of the length-scale estimates without assuming that the distribution is Gaussian.

The lateral and vertical length scales are represented through a single component-scaling vector relative to the streamwise component,

$$(1, \alpha_v, \alpha_w) = \left(1, \mathrm{median}_z\left[\frac{L_v(z)}{L_u(z)}\right], \mathrm{median}_z\left[\frac{L_w(z)}{L_u(z)}\right]\right). \tag{B7}$$

The uncertainty of the scaling coefficients is estimated analogously from the 16th–84th percentile range of the height-wise ratios. This gives a single scaling vector for the TurbSim sensitivity case while retaining the observed height dependence of the streamwise length scale.

The resulting lidar-derived base profile is listed in Tab. B1. The median streamwise length scale varies between approximately 50 and $70\ \mathrm{m}$ over the measured height range. The large standard deviations indicate substantial variability between 10-minute windows, which is why the lidar-derived profile is interpreted as a physically motivated sensitivity case rather than as a uniquely correct turbulence parameterisation.

The resulting single component scaling is

$$(1, \alpha_v, \alpha_w) = (1.00, 1.04, 1.20), \tag{B8}$$

with uncertainty margins of approximately

$$(0.00, 0.10, 0.26). \tag{B9}$$

These values are effective scaling factors derived from the selected scanning-lidar inflow periods. They are therefore not interpreted as universal turbulence anisotropy coefficients. The WindCube samples the beam positions sequentially rather than providing simultaneous point measurements of the three turbulent velocity components, so the derived quantities are referred to as effective lidar-derived integral length scales. They are used here only to assess whether the OpenFAST comparison is sensitive to a more physically plausible turbulent length-scale profile.

Table B1. Effective lidar-derived streamwise integral length scale used as the height-dependent base profile for the TurbSim sensitivity case. Values are calculated from the selected OpenFAST inflow periods. $L(z)$ is the median of the valid 10-minute estimates at each height.

Height z [m a.g.l.]	$L(z)$ [m]	Standard deviation [m]	N
40	66.5	92.8	96
50	52.4	98.9	89
60	51.8	101.6	85
70	56.7	98.3	91
80	58.4	96.6	90
90	64.6	92.9	87
100	70.4	82.8	84
110	65.4	77.6	85
120	68.4	71.4	88
130	69.8	73.2	85
140	64.6	73.7	83
150	60.4	71.1	82
160	60.5	71.2	84
180	61.7	77.2	95
200	55.2	76.9	97
220	67.1	73.7	90
240	71.8	70.3	86
260	64.1	72.3	84
280	63.5	71.7	90
300	66.8	76.3	86

Code and data availability. All data is publicly available via the Zenodo database (van Schaik et al., 2025a) doi: https://doi.org/10.5281/zenodo.17804408. With the single exception of the Gotthard Wind Park Turbine Power data, which was used under Non-Disclosure Agreement. This data may be made available under request to the authors for scientific purposes only. The Zenodo database additionally includes open source code for the analytical power prediction tool as well as example codes and instructions to operate the software.

Author contributions. **BvS**: Conceptualisation, Data curation, Formal analysis, Funding acquisition, Investigation, Methodology, Software, Supervision, Validation, Visualisation, Writing - original draft, and Writing - review & editing.

AB: Conceptualisation, Data curation, Formal analysis, Investigation, Methodology, Software, Validation, Visualisation, Writing - original draft, and Writing - review & editing.

CL: Data curation, Formal analysis, Investigation, Methodology, Software, Validation, Visualisation, Writing - original draft, and Writing - review & editing.

HH: Data curation, Investigation, and Supervision.

ML: Conceptualisation, Investigation, Methodology, Project administration, Funding acquisition, Resources, Supervision, Writing - review & editing.

Competing interests. The authors declare no competing interests.

Acknowledgements. This project has received funding from the European Union's Horizon 2020 research and innovation program under the Marie Skłodowska-Curie grant agreement No. 945363.

The authors would like to thank the Azienda Elettrica Ticinese (AET) for their logistical support, and as the providers of their wind turbine data for analysis in this project.

The research published in this publication was carried out with the support of the Swiss Federal Office of Energy SFOE as part of the SWEET consortium EDGE. The authors bear sole responsibility for the conclusions and results presented in this publication

References

Albers, A.: Turbulence and Shear Normalisation of Wind Turbine Power Curve, in: Proceedings of Windguard, https://www.windguard.com/publications-wind-energy-statistics.html?file=files/cto_layout/img/unternehmen/veroeffentlichungen/2010/Power+Curve+Normalisation.pdf, 2010.

Antoniou, I., Cleve, J., and Piperas, A.: Rotor Average wind speed for power curve performance, Tech. rep., Siemens, https://pcwg.org/proceedings/2013-03-12/02-Rotor-Average-wind-speed-for-power-curve-performance-I-Antoniou-J-Cleve-A-Piperas-SWP.pdf, 2013.

Belu, R. and Koracin, D.: Effects of complex wind regimes and meteorlogical parameters on wind turbine performances, in: 2012 IEEE Energytech, pp. 1–6, https://doi.org/10.1109/EnergyTech.2012.6304638, 2012.

Bot, E.: Flow analysis with nacelle-mounted LiDAR, Tech. rep., TNO, Sint Maartensvlotbrug, The Netherlands, https://publications.tno.nl/publication/34629395/v931oD/e16041.pdf, 2016.

Choukulkar, A., Pichugina, Y., Clack, C. T., Calhoun, R., Banta, R., Brewer, A., and Hardesty, M.: A new formulation for rotor equivalent wind speed for wind resource assessment and wind power forecasting, Wind Energy, 19, 1439–1452, https://doi.org/10.1002/we.1929, 2016.

Clifton, A. and Wagner, R.: Accounting for the effect of turbulence on wind turbine power curves, J. Phys.: Conf. Ser., 524, 012 109, https://doi.org/10.1088/1742-6596/524/1/012109, 2014.

Elliott, D. L. and Cadogan, J. B.: Effects of wind shear and turbulence on wind turbine power curves, in: Presented at the European Community Wind Energy Conference and Exhibition, edited by Kareem, A., pp. 10–14, 1990.

Emeis, S.: How well does a power law fit to a diabatic boundary-layer wind profile?, DEWI-Magazin, 14, 59–62, 12.02.01; LK 01, 2005.

Gasser, J., van Schaik, B. J., Huwald, H., and Lehning, M.: Wind turbine performance in high-alpine terrain as influenced by temperature, snow cover and turbulence, Energy Reports, 15, 109 322, https://doi.org/10.1016/j.egyr.2026.109322, 2026.

IEC: 12-1:Power performance measurements of electricity producing wind turbines, TC 88 Wind energy generation systems, 2022.

Jonkman, J.: The New Modularization Framework for the FAST Wind Turbine CAE Tool, in: 51st AIAA Aerospace Sciences Meeting including the New Horizons Forum and Aerospace Exposition, NRL, https://doi.org/10.2514/6.2013-202, _eprint: https://arc.aiaa.org/doi/pdf/10.2514/6.2013-202, 2013.

Letizia, S., Bodini, N., Brugger, P., Scholbrock, A., Hamilton, N., Porté-Agel, F., Doubrawa, P., and Moriarty, P.: Holistic scan optimization of nacelle-mounted lidars for inflow and wake characterization at the RAAW and AWAKEN field campaigns, Journal of Physics: Conference Series, 2505, 012 048, https://doi.org/10.1088/1742-6596/2505/1/012048, 2023.

Mata, S. A., Pena Martínez, J. J., Bas Quesada, J., Palou Larrañaga, F., Yadav, N., Chawla, J. S., Sivaram, V., and Howland, M. F.: Modeling the effect of wind speed and direction shear on utility-scale wind turbine power production, Wind Energy, 27, 873–899, https://doi.org/10.1002/we.2917, 2024.

Murphy, P., Lundquist, J. K., and Fleming, P.: How wind speed shear and directional veer affect the power production of a megawatt-scale operational wind turbine, WES, 5, 1169–1190, https://doi.org/10.5194/wes-5-1169-2020, 2020.

Niayifar, A. and Porté-Agel, F.: A new analytical model for wind farm power prediction, J. Phys.: Conf. Ser., 625, 012 039, https://doi.org/10.1088/1742-6596/625/1/012039, 2015.

Redfern, S., Olson, J. B., Lundquist, J. K., and Clack, C. T. M.: Incorporation of the Rotor-Equivalent Wind Speed into the Weather Research and Forecasting Model's Wind Farm Parameterization, Monthly Weather Review, 147, 1029 – 1046, https://doi.org/10.1175/MWR-D-18-0194.1, 2019.

Rettenmeier, A., Anger, J., Bischoff, O., Hofsäß, M., Schlipf, D., and Würth, I.: Nacelle-based lidar systems, Remote Sensing for Wind Energy, DTU Wind Energy-E-Report-0029 (EN), pp. 157–170, 2013.

Rosmin, N., Watson, S. J., and Tompson, M.: Power Limitation at High Wind Speeds for a Variable Speed Fixed Pitch Wind Turbine Using Closed-Loop Scalar Control, in: International Conference on Renewable Energies and Power Quality (ICREPQ'10), Granada (Spain), 23th to 25th March, 2010, vol. 165, pp. 1043–1046, 2010.

Sakagami, Y., Santos, P. A., Haas, R., Passos, J. C., and Taves, F. F.: Effects of turbulence, wind shear, wind veer, and atmospheric stability on power performance: a case study in Brazil, EWEA Annual Event, 2015.

Sedaghat, A., Gaith, M., Khanafer, K., and Bani-Hani, E.: Rated wind speed reality or myth for optimization in design of wind turbines, in: 2016 Eleventh International Conference on Ecological Vehicles and Renewable Energies (EVER), pp. 1–4, https://doi.org/10.1109/EVER.2016.7476402, 2016.

Stull, R. B.: An Introduction to Boundary Layer Meteorology, Atmospheric and Oceanographic Sciences Library, 13, Springer Netherlands, Dordrecht, 1st ed. 1988. edn., ISBN 94-009-3027-5, publication Title: An Introduction to Boundary Layer Meteorology, 1988.

Troldborg, N., Andersen, S. J., Hodgson, E. L., and Meyer Forsting, A.: Brief communication: How does complex terrain change the power curve of a wind turbine?, WES, 7, 1527–1532, https://doi.org/10.5194/wes-7-1527-2022, 2022.

Vahidzadeh, M. and Markfort, C. D.: Modified Power Curves for Prediction of Power Output of Wind Farms, Energies, 12, https://doi.org/10.3390/en12091805, 2019.

Vahidzadeh, M. and Markfort, C. D.: An Induction Curve Model for Prediction of Power Output of Wind Turbines in Complex Conditions, Energies, 13, https://doi.org/10.3390/en13040891, 2020.

VAISALA: WindCube v2.1 Specification Sheet and User Manual, Tech. rep., VAISALA France, 2023.

Van Sark, W. G., Van der Velde, H. C., Coelingh, J. P., and Bierbooms, W. A.: Do we really need rotor equivalent wind speed?, Wind Energy, 22, 745–763, https://doi.org/10.1002/we.2319, 2019.

van Schaik, B., Lehning, M., and Huwald, H.: Sequential Wind-Doppler LiDAR wind profile measurements on the Gotthard pass in Switzerland - Summer 2023, https://doi.org/10.5281/zenodo.14524723, 2024.

van Schaik, B., Baruzier, A., Loyer, C., Huwald, H., and Lehning, M.: A Novel Analytical Tool to Capture Wind Profile Variability for Wind Energy Assessment: Fast, Simple, and Beyond State-of-the-Art in Complex Terrain, https://doi.org/10.5281/zenodo.17804408, 2025a.

van Schaik, B., Huwald, H., and Lehning, M.: Resolving three-dimensional wind velocity fields with sequential wind-Doppler LiDAR for wind energy in the complex terrain-Gotthard Pass, Switzerland, Open Res. Eur., 5, 9, https://doi.org/10.12688/openreseurope.19095.3, publisher: F1000 Research Limited, 2025b.

Wagner, R., Antoniou, I., Pedersen, S. M., Courtney, M. S., and Jørgensen, H. E.: The influence of the wind speed profile on wind turbine performance measurements, Wind Energy, 12, 348–362, https://doi.org/10.1002/we.297, 2009.

Wagner, R., Courtney, M., Gottschall, J., and Lindelöw-Marsden, P.: Accounting for the speed shear in wind turbine power performance measurement, Wind Energy, 14, 993–1004, https://doi.org/10.1002/we.509, 2011.

Wagner, R., Cañadillas, B., Clifton, A., Feeney, S., Nygaard, N., Poodt, M., Martin, C. S., Tüxen, E., and Wagenaar, J. W.: Rotor equivalent wind speed for power curve measurement – comparative exercise for IEA Wind Annex 32, J. Phys.: Conf. Ser., 524, 012 108, https://doi.org/10.1088/1742-6596/524/1/012108, 2014.

wind-turbine-models.com: Enercon E-92 - 2.35 MW - Wind Turbine, https://en.wind-turbine-models.com/turbines/131-enercon-e-92, accessed: 2026-05-27, 2026.